POLITECNICO DI TORINO

Master of Science in Automotive Engineering

Master Thesis

Energy Constrained Race Strategies for Formula E Cars

Supervisors

Prof. Ezio Spessa

Prof. Federico Miretti

Candidate

Mohamad Shehadeh

Academic Year 2023-2024

Abstract

This thesis aims to explore the optimal control problem of achieving the minimum lap time considering energy consumption restrictions for a Formula E car. The approach involves initially creating a detailed track and vehicle model. These models will then be utilized in solving the lap time minimization problem using IPOPT optimization software, treating it as a nonlinear programming (NLP) task for effective handling of large-scale optimization. Subsequently, the numerical model's validity will be assessed through road tests, along with an examination of results and variations stemming from different modelling approaches. Lastly, a parametric analysis will be conducted to explore how key vehicle performance parameters affect overall performance.

Acknowledgements

I want to extend my deepest gratitude to my supervisors, Professor Ezio Spessa and Professor Federico Miretti for suggesting a topic that allowed me to derive immense pleasure from the completion of this work, and for all the support provided during its development. Your expertise, encouragement, and commitment have played a pivotal role in shaping this research and fostering my personal and academic development.

I am also grateful to my family for all the support given. To my father, mother, sister, and brother thank you for all the support throughout my academic journey. Their unwavering faith in me has been a constant source of strength and motivation.

Lastly, I would like to express my gratitude to all my friends for their support, encouragement, and understanding during this challenging yet fulfilling journey.

Table of Contents

List of Tables

List of Figures

Chapter 1

Introduction

Motorsport has historically served as a platform for automobile manufacturers to showcase their technological advancements. In recent years, electric car popularity has increased dramatically. Energy management has long been a popular topic with those cutting-edge electric cars. In this regard, the Federation Internationale de l'Automobile (FIA) established the Formula E race championship in 2014 intending to promote these profound technological advancements even more[1]. In addition to offering a compelling environment for research and development aimed at optimizing the performance of electric vehicles[2], Formula E, as a new motorsport category for exclusively electric road vehicles, also serves as an essential testing ground for the digitization of race competitiveness[3].

In Formula E, energy management is paramount, with governing bodies imposing upper limits on power and energy to ensure fair competition such as limitations on the power output from a vehicle's Rechargeable Energy Storage System (RESS), which can differ across various events such as qualifying or races. Additionally, there are constraints on the quantity of energy that can be supplied to the Motor Generator Unit (MGU)[4]. Consequently, drivers and engineers must balance lap time optimization with energy constraints, making energy management a pivotal aspect of competitive race strategy in Formula E events.

Formula E has evolved through three generations, each marked by significant advancements [5]. The first generation (2014-2018) featured standardized chassis and batteries, while the second generation (2018-2022) introduced sleeker designs and increased power. Now, with the third generation (2022-present), known as Gen3, Formula E cars boast lighter, more efficient powertrains and a commitment to sustainability. This evolution reflects Formula E's rapid growth as a platform for showcasing electric vehicle technology and driving progress towards a cleaner, more sustainable future.

Table 1.1: Specifications of different generations of Formula-E cars [6] [5].

Generation	Weight	Battery capacity	Drive type	Max power	Top speed
Gen 1	880 kg	28 kWh	Rear wheel drive	200 kW	225 kMh
Gen 2	900 kg	52 kWh	Rear wheel drive	250 kW	280 kMh
Gen 3	856 kg	51 kWh	Rear wheel drive Front & rear axle regeneration	350 kW	322 kMh

Lap time simulation (LTS) holds significant value for racing teams as it enables the simulation of a single race car equipped with a specific setup for one lap on a designated racetrack. Beyond

Figure 1.1: Formula E Gen 3 Car [7]

merely calculating lap times, LTS also yields additional insights, such as energy consumption. Understanding a vehicle's maximum performance capabilities aids teams in comprehending its behaviour on any racetrack, even before building the car. Thus, the ability to simulate the impacts of various energy management strategies on both lap time and energy consumption is crucial for achieving the optimal balance. Typically, LTS overlooks long-term effects like energy loss, which are addressed in race simulations that encompass an entire race and inform race strategy decisions[3]. Nonetheless, these two simulation types collaborate closely, as LTS provides many necessary parameters for race simulations, such as lap time mass sensitivity. Therefore, co-simulation alongside a race simulation presents another practical application for LTS.

The aim of this thesis is to develop a lap time simulation to optimize the race line considering the energy consumption limits. This problem is commonly known as the Minimum Lap Time Problem (MLTP). The selected solution method is based on the optimal control approach and uses direct collocation, taking advantage of the framework Casadi[8] and the solver IPOPT[9] to define and solve the optimisation problem.

Lap Time Simulation is structured into three parts. The first section delineates the modelling of both racetrack and vehicle components. The subsequent section elucidates the formulation of the optimization problem as an Optimal Control Problem (OCP) and its transcription into a Non-Linear Program (NLP). The final section presents the outcomes yielded by the simulation. Due to the unavailability of team-specific data, our simulation is designed to be adaptable, drawing upon publicly accessible sources like onboard video streams and lap times. This flexible design enables its utility across diverse circuit racing series.

Chapter 2

Background

2.1 Formula E

Formula E comprises 11 teams, with each team fielding two drivers who compete against each other in a championship consisting of 12 to 14 races throughout the season. There are two championship titles at stake: the Constructors' Championship and the Drivers' Championship. The Constructors' Championship is awarded to the team that accumulates the highest points across the season, regardless of whether their drivers individually win the Drivers' Championship. Points are awarded to the top 10 finishers, with additional points given for securing pole position and setting the fastest lap during the race.

1ST	DRIVER #01	+25 pts
2ND	DRIVER #33	+18 pts
3RD	DRIVER #58	+15 pts
4TH	DRIVER #10	+12 pts
5TH	DRIVER #37	+10 pts
6TH	DRIVER #48	+8 pts
7TH	DRIVER #05	+6 pts
8TH	DRIVER #25	+4 pts
9TH	DRIVER #16	+2 pts
10T	DRIVER #03	+1 pts

Figure 2.1: Calculation of Formula E points [7]

During a typical race weekend, there are usually two practice sessions held on the same day. On the following day, qualifying takes place, determining the starting grid for the race. This format is common when a city hosts only one ePrix event.

However, in cities where two ePrix events are held like Misano eprix, the race weekend format is modified. On the first day, there is a lone practice session. On the subsequent day, the second practice session and qualifying occur, followed by the first ePrix. The third day repeats the format of the second day, with a third practice session, qualifying, and the race.

This format allows for efficient use of the race weekend schedule and ensures that spectators have ample opportunities to witness the on-track action and excitement of Formula E racing.

Figure 2.2: Formula E qualifying format [7]

Attack Mode made its Formula E debut for the 2018/2019 season, functioning as a strategic innovation to improve on-track overtaking opportunities[10]. Its debut was intended to mirror the improved overtaking witnessed in Formula One races following the introduction of DRS(Drag Reducing System) in 2011. However, a big incentive for adding Attack Mode was the substantial advancement in battery technology within Formula E cars.

Activating Attack Mode necessitates drivers to drive off the racing line and navigate through the designated Activation Zone as illustrated in Figure 2.3. In exchange for deviating from the ideal racing trajectory around the corner, drivers gain an extra 50 kW of power, boosting their total power output to 350 kW compared to the standard 300 kW. This added power can be harnessed by drivers aiming to enhance their competitiveness and progress their position on the track. The Formula E website [11] states that the duration for which Attack Mode remains active is set by the FIA and disclosed before the race commences.

Each driver is required to activate Attack Mode at least once during a race. Similar to the rules governing DRS in Formula 1, this mode cannot be engaged during the initial two laps of the race. Furthermore, it is prohibited to utilize Attack Mode during full-course yellow flags or when the safety car is deployed. While entering the activation zone may result in drivers temporarily losing positions as they deviate from the optimal racing line, upon exiting the zone, they can leverage the additional power to execute overtakes and extend their lead once again depending on several options to use this additional power as it is shown in Figure 2.4.

Figure 2.3: Activation zone [7]

ATTACK MODE
MINUTES DISTRIBUTION

	OPTION 1	OPTION 2	OPTION 3
USE 1	02:00	03:00	01:00
USE 2	02:00	01:00	03:00

Figure 2.4: Attack mode options [7]

Attack Mode made its Formula E debut for the 2018/2019 season, functioning as a strategic innovation to improve on-track overtaking opportunities[10]. Its debut was intended to mirror the improved overtaking witnessed in Formula One races following the introduction of DRS(Drag Reducing System) in 2011. However, a big incentive for adding Attack Mode was the substantial advancement in battery technology within Formula E cars.

2.2 Literature Review

The challenge of the minimum lap time has long been one that engineers have attempted to solve [12], and there is a wealth of literature on this topic. Rebuilding the state and control trajectories from the highest speed at the apex of the corners is where the earliest references to this date come from. Several approaches have been investigated since then.

Siegler et al.[13] conducted a comparison of three different modelling approaches and determined that both quasi-steady-state and transient methods outperform steady-state modelling. Brayshaw et al.[14] delved deeper into the quasi-steady-state approach by employing optimal control techniques and found its sensitivity to setup changes to be comparable to that of an optimized transient solution. Casanova[15] and Kelly[16] concentrated on achieving minimum lap time targets using purely optimal control techniques, with Kelly additionally enhancing robustness by considering stability criteria. Volkl[17] introduced a method for integrating transient modelling into quasi-steady-state calculations, resulting in reduced computation times. Timings et al.[18] developed a LTS based on model predictive control, augmented with a compensatory controller to mitigate driver errors. Perantoni et al.[19] and Limebeer et al.[20] employed 3D racetrack representations to minimize lap time, with Limebeer et al. also addressing time-optimal energy management for F1 hybrid powertrains. However, it's noted that optimizing energy management may not always lead to feasible driving behaviour strategies during a race.

Three basic approaches have emerged as the most effective ways to overcome minimum lap time issues. The first way takes an indirect approach, utilizing Pins software (previously XOptima), as detailed in [21]. This approach has been widely used since the late 1990s, with remarkable results demonstrated in [21, 22, 23]for motorcycle applications and [24, 25] for automobiles. The second strategy employs a direct multiple firing method assisted by MUSCOD-II software, with the most remarkable success reported in [26]. The most recent innovation in this domain is a direct optimum control technique that employs full direct transcription via pseudo-spectral collocation, as demonstrated by GPOPS-II software in [27]. This approach, which was introduced in 2013, is shown to have cutting-edge applications in the field in [28, 29].

Chapter 3

Simulation Environment

3.1 Track Model

The track is represented using a curvilinear coordinate system, departing from conventional xy coordinates. This system tracks the vehicle's position along the arc length of the track's centerline. Such an approach offers a concise means of depicting the vehicle's advancement and ensures its adherence to the track limits[30]. The track model's primary function is to give the solver the track's curvature profile. the track model used in this thesis is adopted from Perantoni and Limebeer [19].

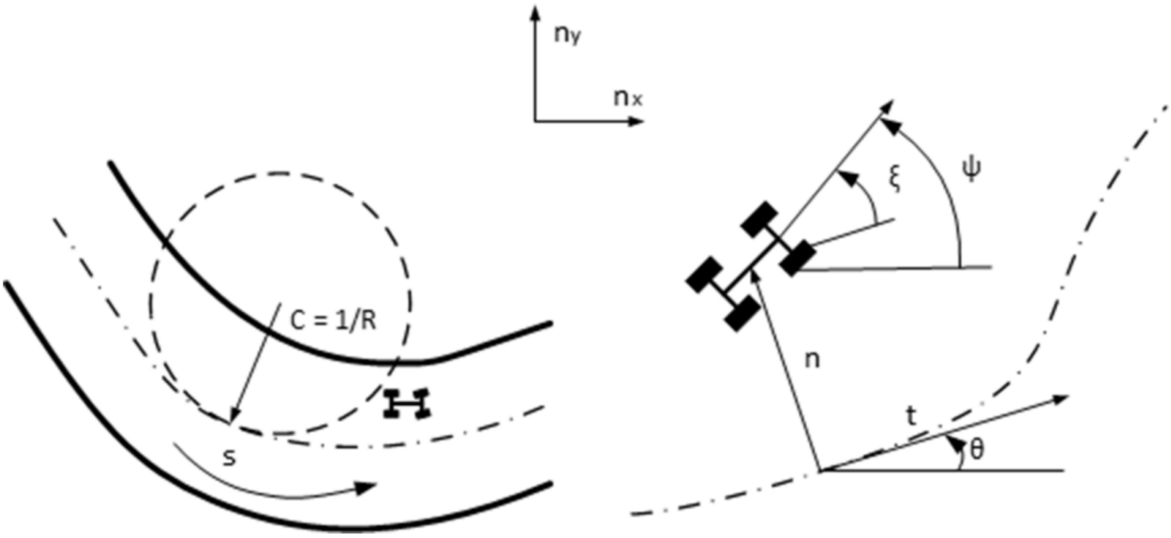

Figure 3.1: Track Modeling Coordinate [6]

The parameters s and n, which indicate the distance traveled along the centerline from the start/finish line and the perpendicular distance of the vehicle mass center from the centerline to the centerline's tangent direction, respectively, can be used to characterize the location of the vehicle on the track, as shown in 3.1.

The track's curvature at any given location s is determined by $C = 1/R$ and its radius of curvature is given by R.

The vehicle's absolute yaw angle the angle between the vehicle and the track is represented by ψ and ξ respectively. Therefore, $\psi = \theta + \xi$, where θ represents the track orientation angle. It is evident that in the typical rectangular inertial system, each increment of progress ds along the track centre line in this coordinate system results in the following increments of dx and dy:

$$dx = ds\ cos(\theta) \tag{3.1}$$

$$dy = ds\ sin(\theta) \tag{3.2}$$

This provides

$$\frac{dy}{dx} = tan(\theta) \tag{3.3}$$

From basic geometry, we can determine that the track curvature is given by

$$C = \frac{d\theta}{ds} = \frac{d}{ds}\left(arctan\frac{dy}{dx}\right) \tag{3.4}$$

It offers a theoretical method for determining the track curvature from GPS data that is stated in rectangular coordinates. The vehicle's velocity can be resolved in the t-direction (see Figure 3.1), which produces

$$\dot{s} - n\dot{\theta} = u\ cos\psi - v\ sin\psi \tag{3.5}$$

where u and v denote for the longitudinal and lateral components of the mass-center velocity of the vehicle, respectively. n, which is in the direction of n, indicates the lateral position of the vehicle's mass center with respect to the track center line; note that $\frac{d(n\theta)}{dt} = n\dot{\theta} + \dot{n}\theta$ with $\dot{n}\theta$ perpendicular to *t*. Identify (3.5) provides

$$\dot{s} = \frac{u\ cos(\xi) - v\ sin(\xi)}{1 - nC} \tag{3.6}$$

The vehicle's location's abscissa point's centerline curvature is indicated by C. When the car is on the left side of the centerline during a left turn, C is positive and n is positive. Note that the dot notation indicates that these are time derivatives. As cars aren't meant to drive backwards on a track in a realistic manner, the traveled distance, s, is a monotonically increasing function of time. s is included as an independent variable in the optimal control problem (OCP) with the goal of minimizing the lap time t.

The rate of change of *n* using (3.4) is given by

$$\dot{n} = u\ sin(\xi) + v\ cos(\xi) \tag{3.7}$$

Finally, differentiating $\psi = \xi + \theta$ using (3.4)with respect to time in

$$\dot{\xi} = \dot{\psi} - C\dot{s} \tag{3.8}$$

The relationship between "time" and "distance traveled" suggests that either can be eliminated when formulating optimal control problems. Opting for "distance traveled" as the independent variable offers benefits, including maintaining a direct link with track position and reducing the number of problem variables by one. To implement this change, it's crucial to establish a one-to-one correspondence between distance s and time t. Given that $ds = \dot{s}dt$, all that has to be done is make sure the vehicle velocity is positive in the track-tangent direction; this will be assumed going forward. Following this, we note that

$$dt = \frac{dt}{ds}ds = S_f(s)ds \tag{3.9}$$

where S_f comes from (3.6) as follows

$$S_f = (\frac{ds}{dt})^{-1} = \frac{1 - nC}{u\ cos(\xi) - v\ sin(\xi)} \tag{3.10}$$

The value S_f represents the inverse of the vehicle velocity component aligned with the track's tangent direction (on the centre line at position s). This establishes a direct correspondence between s and t when both the numerator and denominator are positive. Opting for "distance traveled" as the independent variable using (3.7) yields

$$\frac{dn}{ds} = S_f\ (u\ sin(\xi) + v\ cos(\xi)) \tag{3.11}$$

from (3.8), and

$$\frac{d\xi}{ds} = S_f w - C \tag{3.12}$$

where $w = \dot{\psi}$ is the vehicle yaw rate.

A 2D map, which is defined by the coordinates or function representing the track bounds, is the most fundamental representation of a racetrack. Further details such as variable coefficients of friction (as detailed in [31]), road camber, gradient, or surface elevation changes can be incorporated. As presented in [32], More advanced models begin by portraying the track as a strip, a 2D surface within 3D space. A 2D representation of the track is selected for this investigation.

3.2 Vehicle Model

The level of complexity provided for the vehicle dynamic model determines the possibility of obtaining realistic solutions for the optimal control problem, or rather results that can be assumed as a good approximation of the real behavior of the vehicle. The more the model can capture the most important dynamic parameters, the more the simulation is capable of reaching the ideal perfect performance for the real vehicle, in terms of minimum time manoeuvres.

Pitch and roll motions were not used in this thesis to apply higher-fidelity models since they are more significant in jobs where vehicle dynamics research predominates. Because the suspensions on Formula One and Formula E cars are so rigid, the roll and pitch movements in these high-level motorsports have very small amplitudes. These are significant primarily because they have a significant impact on aerodynamic performance, as exemplified by Formula One, where aerodynamic downforce character is a dominant factor that cannot be disregarded in performance analysis[29]. Conversely, in Formula E, teams utilize identical bodywork with a design concept distinct from Formula One, resulting in less emphasis on downforce generation. Consequently, the performance in Formula E is less dependent or sensitive to pitch and roll motions [6].

In this thesis, the vehicle is modelled with seven degrees of freedom (DOFs), namely the longitudinal, lateral, and yaw motions, along with four-wheel rotations. The model also incorporates aerodynamic loads and considers load transfer. Additionally, a limited-slip differential (LSD) is included in the model, reflecting the single-motor per-axle configuration typical of the cars examined.

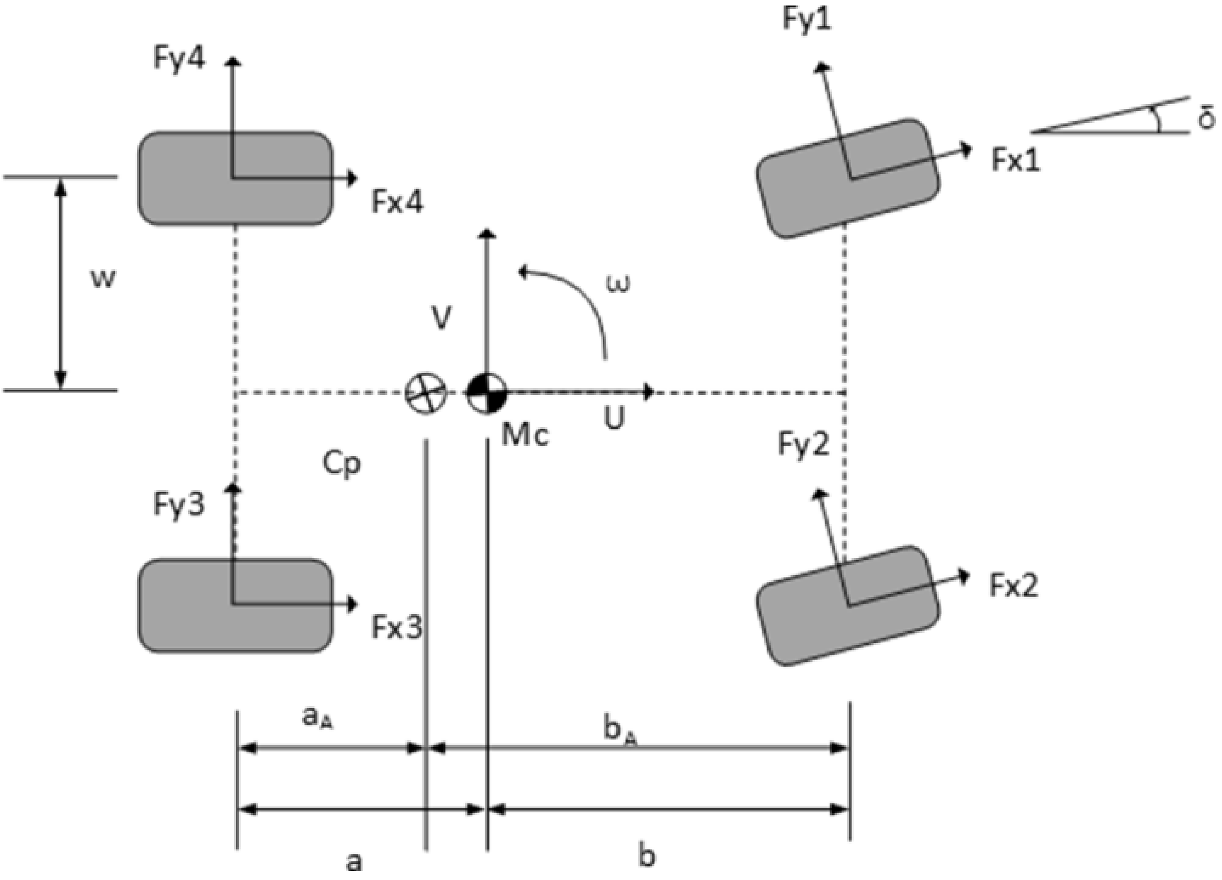

Figure 3.2: 7-DOF Vehicle model [6]

3.2.1 Body dynamics

The longitudinal, lateral and yaw motions are represented by the following equations, as shown in figure 3.2:

$$M\frac{d}{dt}u(t) = Mwv + F_x \tag{3.13}$$

$$M\frac{d}{dt}v(t) = -Mwu + F_y \tag{3.14}$$

$$\begin{aligned} Iz\frac{d}{dt}w(t) =& b(cos(\delta)(F_{y_1} + F_{y_2}) + sin(\delta)(F_{x_1} + F_{x_2})) - w(sin(\delta)F_{y_2} - cos(\delta)F_{x_2}) + \\ & wF_{x_3} - w(cos(\delta)F_{x_1} - sin(\delta)F_{y_1}) - wF_{x_4} - a(F_{y_3} + F_{y_4}) \end{aligned} \tag{3.15}$$

The following is an expression for these equations in terms of the independent variable s

$$\frac{du}{ds} = S_f(s)\dot{u} \tag{3.16}$$

$$\frac{dv}{ds} = S_f(s)\dot{v} \tag{3.17}$$

$$\frac{dw}{ds} = S_f(s)\dot{w} \tag{3.18}$$

In this context, M represents the vehicle's mass, Iz denotes the vehicle's yaw moment of inertia, δ signifies the steering angle of the front wheels, and w refers to the track width. The parameters a and b indicate the distances from the vehicle's center of mass to the front and rear axles, respectively. Additionally, F_{x_i} and F_{y_i} represent the longitudinal and lateral forces, respectively, exerted by the tyres. The subscript i (where i = 1, 2, 3, 4) denotes the specific tyre, with 1 and 2 representing the front left and right tyres and 3 and 4 representing the rear right and left tyres.

The vehicle is being affected by longitudinal and lateral forces, denoted as F_x and F_y, respectively. These forces are provided by

$$F_x = cos(\delta)(F_{x_1} + F_{x_2}) - sin(\delta)(F_{y_1} + F_{y_2}) + (F_{x_3} + F_{x_4}) - F_{a_x} \tag{3.19}$$

$$F_y = cos(\delta)(F_{y_1} + F_{y_2}) + sin(\delta)(F_{x_1} + F_{x_2}) + (F_{y_3} + F_{y_4}) \tag{3.20}$$

where F_{a_x}, is the vehicle's longitudinal aerodynamic load.

3.2.2 Wheel dynamics

At the points where the tyres make contact with the ground, the tyre forces exert normal, longitudinal, and lateral forces on the vehicle's chassis, causing a reaction in the inertial frame. The forces vary based on the normal load and the longitudinal and lateral slip of the tyres. The steering is done by the front wheels only, as shown in Figure 3.2.

An empirical tyre model[33] is employed, featuring linearized interpolation to determine the peak values of longitudinal and lateral friction coefficients[16].

Table 3.1: Description of symbols.

Symbol	Description	Front value	Rear value
F_{z_R1}	Reference normal load 1	2000 N	2000 N
F_{z_R2}	Reference normal load 2	6000 N	6000 N
$\mu_{x_{max1}}$	Peak longitudinal friction coefficient at load 1	1.4	1.75
$\mu_{x_{max2}}$	Peak longitudinal friction coefficient at load 2	1.12	1.4
κ_{max_1}	Slip coefficient for the friction peak at load 1	0.11	0.11
κ_{max_2}	Slip coefficient for the friction peak at load 2	0.10	0.10
$\mu_{y_{max_1}}$	Peak lateral friction coefficient at load 1	1.62	1.8
$\mu_{y_{max_2}}$	Peak lateral friction coefficient at load 2	1.3	1.45
α_{max_1}	Slip angle for the friction peak at load 1	9°	9°
α_{max_2}	Slip angle for the friction peak at load 2	8°	8°
Q_x	Longitudinal shape factor	1.9	1.9
Q_y	Lateral shape factor	1.9	1.9

The following provides the longitudinal and lateral forces:

$$F_{x_i} = \mu_{x_i} F_{z_i} \frac{\kappa_{n_i}}{\sqrt{\alpha_{n_i}^2 + \kappa_{n_i}^2 + \epsilon}} \tag{3.21}$$

$$F_{y_i} = \mu_{y_i} F_{z_i} \frac{\alpha_{n_i}}{\sqrt{\alpha_{n_i}^2 + \kappa_{n_i}^2 + \epsilon}} \tag{3.22}$$

κ_{n_i} and α_{n_i} represent the normalized tyre slip with regard to the slip value where the peak friction coefficient occurs, and F_{z_i} is the tyre normal force:

$$\alpha_{n_i} = \frac{\alpha_i}{\alpha_{max_i}} \tag{3.23}$$

$$\kappa_{n_i} = \frac{\kappa_i}{\kappa_{max_i}} \tag{3.24}$$

The slip angles α_i and ratios κ_i are defined as:

$$\alpha_1 = \delta - arctan(\frac{v + wa}{u - w\mathrm{w}}),\ \kappa_1 = -1 + \frac{Rw_1}{cos(\delta)(u - w\mathrm{w}) - sin(\delta)(v + wa)} \tag{3.25}$$

$$\alpha_2 = \delta - arctan(\frac{v + wa}{u + w\mathrm{w}}),\ \kappa_2 = -1 + \frac{Rw_2}{cos(\delta)(u + w\mathrm{w}) - sin(\delta)(v + wa)} \tag{3.26}$$

$$\alpha_3 = -arctan(\frac{v - wb}{u + w\mathrm{w}}),\ \kappa_3 = -1 + \frac{Rw_3}{u + w\mathrm{w}} \tag{3.27}$$

$$\alpha_4 = -arctan(\frac{v - wb}{u - w\mathrm{w}}),\ \kappa_4 = -1 + \frac{Rw_4}{u - w\mathrm{w}} \tag{3.28}$$

where R is the tyre radius and w_i is the angular velocity of each wheel.

Linear interpolation is utilized to determine the peak friction values, treating them as linear functions of the tyre's normal loads. The meanings of the symbols are detailed in Table 3.1.

$$\mu_{x_{max}} = (F_z - F_{z_R}1)(\frac{\mu_{x_{max2}} - \mu_{x_{max1}}}{F_{z_R}2 - F_{z_R}1}) + \mu_{x_{max1}} \tag{3.29}$$

$$\mu_{y_{max}} = (F_z - F_{z_R}1)(\frac{\mu_{y_{max2}} - \mu_{y_{max1}}}{F_{z_R}2 - F_{z_R}1}) + \mu_{y_{max1}} \tag{3.30}$$

$$\kappa_{max} = (F_z - F_{z_R}1)(\frac{\kappa_{max_2} - \kappa_{max_1}}{F_{z_R}2 - F_{z_R}1}) + \kappa_{max_1} \tag{3.31}$$

$$\alpha_{max} = (F_z - F_{z_R}1)(\frac{\alpha_{max_2} - \alpha_{max_1}}{F_{z_R}2 - F_{z_R}1}) + \alpha_{max_1} \tag{3.32}$$

Following that, the descriptions of the longitudinal and lateral friction coefficients in equations (3.21) and (3.22) are provided by

$$\mu_{x_i} = \mu_{x_{imax}} sin\left(Q_x arctan\left(\frac{\pi}{2arctan(Q_x)}\sqrt{\alpha_{n_i}^2 + \kappa_{n_i}^2}\right)\right) \tag{3.33}$$

$$\mu_{y_i} = \mu_{y_{imax}} sin\left(Q_y arctan\left(\frac{\pi}{2arctan(Q_x)}\sqrt{\alpha_{n_i}^2 + \kappa_{n_i}^2}\right)\right) \tag{3.34}$$

where Q_x and Q_y represent shaping factors.

The OCP computation time can be shortened by reducing the tyre model in this fashion, but several crucial characteristics of a race tyre must still be considered. These include: 1) nonlinear tyre characteristics regarding tyre slip, 2) fluctuations in peak friction coefficients resulting from alterations in normal force, and 3) incorporation of combined slip and shaping factors for determining friction coefficients. It is important to highlight that in equations (3.21) and (3.22), a small value denoted as ϵ is included in the denominator of the combined-slip coefficient. This addition prevents scenarios of zero-slip, which could result in an infinite gradient derivative, causing challenges for the OCP solver. However, this value should be sufficiently small (10e-06) to ensure the accuracy of the tyre model is maintained.

The torques of the motors are transmitted to the driving wheels by the LSD(Limited-Slip Differential) and the drive shafts. The LSD torque is transmitted from the wheel rotating at a higher speed to the slower wheel.

This torque is expressed as follows:

$$T_{diff} = 0.5k_d(w_{inner} - w_{outer}) \tag{3.35}$$

with w_{inner} and w_{outer} represent the angular velocities of the inner and outer wheels on the same axle, respectively, while k_d denotes the rotational damping coefficient of the LSD.

Lastly, the motions of the wheels are delineated as follows:

$$J_w\dot{w}_1 = k_b(T_{brake} + \frac{T_{regen}}{4}) + T_{diff-f} - F_{x1}R \tag{3.36}$$

$$J_w\dot{w}_2 = k_b(T_{brake} + \frac{T_{regen}}{4}) - T_{diff-f} - F_{x2}R \tag{3.37}$$

$$J_w\dot{w}_3 = T_{drive} + (1 - k_b)(T_{brake} + \frac{T_{regen}}{4}) - T_{diff-r} - F_{x3}R \tag{3.38}$$

$$J_w\dot{w}_4 = T_{drive} + (1 - k_b)(T_{brake} + \frac{T_{regen}}{4}) + T_{diff-r} - F_{x4}R \tag{3.39}$$

The wheel rotational inertia is represented by J_w, the brake bias to the front by k_b, and the drive torque and brake torque, respectively, are derived from the motor brake torque produced by the caliper or the motor regeneration. T_{regen} is extra regenerative torque that is applied to the steering wheel by the driver.

To prevent pedal overlap, these three torques are constrained by:

$$T_{drive}T_{brake} = 0 \tag{3.40}$$

$$T_{drive}T_{regen} = 0 \tag{3.41}$$

The drive power, denoted as P_{drive}, and the regeneration power, referred to as P_{regen}, are determined by:

$$P_{drive} = (T_{drive} + T_{diff-r})w_4 + (T_{drive} - T_{diff-r})w_3 \tag{3.42}$$

$$\begin{aligned} P_{regen} =& (T_{regen} + T_{diff-r})w_4 + (T_{regen} - T_{diff-r})w_3 + \\ & (T_{regen} + T_{diff-f})w_1 + (T_{regen} - T_{diff-f})w_2 \end{aligned} \tag{3.43}$$

3.2.3 Normal tyre loads

At every time step, it is necessary to compute the normal forces acting on the tyres for the calculation of longitudinal and lateral tyre forces. These forces must adhere to the fundamental equilibrium equations of the vehicle. In the vertical direction:

$$F_{z1} + F_{z2} + F_{z3} + F_{z4} + = Mg - F_{az} = 0 \tag{3.44}$$

F_{zi} represents the normal force exerted on each tyre, M denotes the overall vehicle mass, g signifies the acceleration due to gravity, and F_{az} indicates the aerodynamic vertical load acting on the vehicle. To ensure equilibrium at the moment around the x-axis of the vehicle, as depicted in Figure 3.2:

$$\mathrm{w}(F_{z4} - F_{z3}) + \mathrm{w}(F_{z1} - F_{z2}) + F_y = 0 \tag{3.45}$$

To maintain the vehicle's current equilibrium around its y-axis:

$$b(F_{z3} + F_{z4}) - a(F_{z1} + F_{z2}) - hF_x - (a_a - a)F_{az} = 0 \tag{3.46}$$

where h represents the height of the vehicle mass center to the ground.

The lateral load transfer bias D is added to the following balancing equation to guarantee a distinct solution for each of the four normal forces. The distribution of lateral load transmission between the front and rear axles is described as follows:

$$D((F_{z2} + (F_{z3} - (F_{z1} - (F_{z4}) - F_{z2} + F_{z1} = 0 \tag{3.47}$$

F_{zi} is the tyre's normal force and it is computed, considering the static weight of each axle (where g represents the acceleration due to gravity and l denotes the wheelbase length), the longitudinal load transfer $\lceil_x$, and the downforce F_{az} (equally distributed between both axles).

$$F_{zi} = Mg\frac{l_i}{l} \pm \lceil_x + \frac{F_{az}}{2} \tag{3.48}$$

The model considers load transfer in a quasi-steady state, without taking into account suspension geometry, springs and dampers, or chassis stiffness, which would affect the dynamic equations. The algebraic loop arises from the relationship between vertical load, load transfer, and tyre forces. To resolve this issue, load transfer is treated as a distinct optimization variable subject to the following constraint:

$$\lceil_x = ((F_{x1} + F_{x2})cos(\delta) - (F_{y1} + F_{y2})sin(\delta) + F_{x3} + F_{x4} - F_{ax})\frac{h}{l} \tag{3.49}$$

The model accounts for the combined behaviour of the tyres by constraining the total longitudinal and lateral forces to the friction circle, which is given by the friction coefficient. Employing same mu value for both lateral and longitudinal forces simplifies the constraint:

$$\mu_i^2 - \frac{F_{x,i}^2 + F_{y,i}^2}{F_{z,i}^2} \geq 0 \tag{3.50}$$

The aerodynamics loads F_{az} and F_{ax} are privoded by:

$$F_{az} = 0.5 C_l \rho_a A u^2 \tag{3.51}$$

$$F_{ax} = 0.5 C_d \rho_a A u^2 \tag{3.52}$$

where C_d represents the aerodynamic drag coefficient, C_l denotes the lift coefficient, ρ_a signifies the air density and A stands for the frontal area of the vehicle.

Chapter 4

Optimisation Problem

The best racing lines and controls can be found concurrently when using the optimum control strategy to solve a problem that considers the transient behaviour of comprehensive dynamic models. Frequently, optimal control and trajectory optimization are considered synonymous, as their techniques and implementations can essentially be identical. Optimal control methodologies are typically categorized into direct and indirect approaches[34]. After formulating the MLTP as an OCP, indirect methods strive to identify the requisite conditions for optimality, while direct orthogonal collocation converts it into a discrete minimization problem, often referred to as NLP (non-linear program). This section outlines the steps taken to discretize and formulate the optimization problem, as well as the eventual implementation.

4.1 Trajectory Optimisation

Formally, an optimal control problem is presented as follows: Find the state (or trajectory) $x(t) \in \mathbb{R}^n$, the control $u(t) \in \mathbb{R}^m$, the static parameter vector $\mathbf{p} \in \mathbb{R}^q$, the initial time $t_0 \in \mathbb{R}$, and the terminal time $t_f \in \mathbb{R}$ (where t belongs to the interval $[t_0, t_f]$) that optimizes the performance index[35].

$$J = \Phi[\mathbf{x}(t_0), t_0, \mathbf{x}(t_f), t_f; \mathbf{p}] + \int_{t_0}^{t_f} L[\mathbf{x}(t), \mathbf{u}(t), t; \mathbf{p}]\, dt \tag{4.1}$$

Constrained by the dynamic limitations (specifically, constraints represented by differential equations),

$$\dot{\mathbf{x}}(t) = \mathbf{f}[\mathbf{x}(t), \mathbf{u}(t), t; \mathbf{p}], \tag{4.2}$$

where the path constraints are represented by

$$\mathbf{C}_{\text{min}} \leq \mathbf{C}[\mathbf{x}(t), \mathbf{u}(t), t; \mathbf{p}] \leq \mathbf{C}_{\text{max}}, \tag{4.3}$$

with boundary conditions are given by

$$\phi_{\text{min}} \leq \phi[\mathbf{x}(t_0), t_0, \mathbf{x}(t_f), t_f; \mathbf{p}] \leq \phi_{\text{max}} \tag{4.4}$$

Each component of the state, control, and static parameter can be expressed as

$$\mathbf{x}(t)=\begin{bmatrix}x_1(t)\\ \vdots\\ x_n(t)\end{bmatrix};\quad \mathbf{u}(t)=\begin{bmatrix}u_1(t)\\ \vdots\\ u_m(t)\end{bmatrix};\quad \mathbf{p}=\begin{bmatrix}p_1\\ \vdots\\ p_q\end{bmatrix} \tag{4.5}$$

Equation (4.2) presents a differential equation that characterizes the dynamics of the system, and the performance index measures the trajectory's quality. A lower value of J is preferred when the objective is to minimize the performance index. Conversely, a greater value of J is considered preferable when the goal is to maximize the performance index. A multi-phase optimal control problem is presented as follows:

Optimize the cost

$$J=\sum_{k=1}^{P} J^{(k)} \tag{4.6}$$

The cost function in each phase,$J^{(k)}$, $(k=1,\ldots,P)$, follows the structure described in Equation (4.1), while adhering to the dynamic constraints.

$$\dot{\mathbf{x}}^{(k)}(t)=\mathbf{f}\left(\mathbf{x}^{(k)}(t),\mathbf{u}^{(k)}(t),\mathbf{p}^{(k)},t\right) \tag{4.7}$$

where the boundary conditions are

$$\phi_{\min}^{(k)}\leq\phi^{(k)}\left(\mathbf{x}^{(k)}(t_0^{(k)}),t_0^{(k)},\mathbf{x}^{(k)}(t_f^{(k)}),\mathbf{p}^{(k)},t_f^{(k)}\right)\leq\phi_{\max}^{(k)} \tag{4.8}$$

and the algebraic path constraints

$$C_{\min}^{(k)}\leq C^{(k)}\left(\mathbf{x}^{(k)}(t),\mathbf{u}^{(k)}(t),\mathbf{p}^{(k)},t\right)\leq C_{\max}^{(k)} \tag{4.9}$$

with the linkage constraints

$$\mathbf{L}_{\min}^{(s)}\leq\mathbf{L}\left(\mathbf{x}^{(ls)}(t_f^{(ls)}),\mathbf{u}^{(ls)}(t_f^{(ls)}),\mathbf{p}^{(ls)},t_f^{(ls)},\mathbf{x}^{(rs)}(t_f^{(rs)}),\mathbf{u}^{(rs)}(t_f^{(rs)}),\mathbf{p}^{(rs)},t_f^{(rs)}\right)\leq\mathbf{L}_{\max}^{(s)} \tag{4.10}$$

The parameter S represented in Eq.(4.10) the number of pairs of phases to be linked, where $r_s\in[1,\ldots,S]$ and $l_s\in[1,\ldots,S]$ denote the right and left phases, respectively, of the linked pairs. Here, $r_s\neq l_s$ (indicating that a phase cannot be linked to itself), and $s\in[1,\ldots,S]$.

For the MLTP problem, when time is utilized as the independent variable, the integrand of the Lagrange term would be set to 1. However, in this study, distance replaces time as the independent variable, leading to the definition of the integral objective function as follows:

$$J(w)=\int_{t_0}^{t_f}1\ .\ dt=\int_{s_0}^{S_f(w)}S_f(w)\ .\ ds \tag{4.11}$$

where t_f and s_f denote the final time and distance, respectively, and w contains the optimization variables. Typically, these optimization variables consist of the states x, the control inputs u, and a finite number of static parameters p. In addition, an extra continuous variable y is included to accommodate auxiliary continuous variables that are neither states nor inputs, such as load transfer. Unlike previous studies where load transfer was integrated by expanding the input vector, this new formulation provides more flexibility in handling the corresponding decision variables of the NLP. For example, it allows for the approximation of y with higher-order polynomials compared to the inputs.

The limitations of the OCP can be represented as

$$\frac{d}{ds}\mathbf{x} = \mathbf{f}(\mathbf{w}) \tag{4.12}$$

$$\mathbf{h}(\mathbf{w}) \leq 0 \tag{4.13}$$

$$\mathbf{b}(\mathbf{w}_0, \mathbf{w}_f) \leq 0 \tag{4.14}$$

The system dynamics are governed by Equation (4.12), where f encompasses Equations (3.7), (3.8), (3.13), (3.14), (3.15), (3.36),(3.37),(3.38), and (3.39). h denotes the path constraints, which may include both equality and inequality constraints, such as Equations (3.49), (3.50), (3.40), and (3.41). Boundary constraints, defined by b, are utilized to establish the initial and final states. For instance, these constraints could specify the initial longitudinal speed or the orientation of the vehicle after the track.

Constraints that rely solely on one optimization variable are enforced by setting appropriate bounds for the corresponding decision variables in the NLP. For instance, the lateral distance of the vehicle from the centerline, considered a state in the model, should consistently remain below half the width of the track. Thus, with Λ representing the vehicle width, the state boundaries must be configured as follows:

$$w^2 - \Lambda \geq n \geq -w^2 + \Lambda \tag{4.15}$$

4.2 Transcription

It is important to recognize that setting bounds for decision variables in the NLP differs from defining constraints. While an initial guess must always fall within the bounds, a constraint may not initially be satisfied. Despite the mathematical problem being identical in both scenarios, numerically they are distinct and can affect the solver's performance. In the course of this study's development, it was noted that enforcing the limit for the input brake torque as a constraint, rather than a bound, resulted in quicker simulation times. An intriguing avenue for future research might involve further exploration of this phenomenon.

The conversion of the OCP into a discrete NLP is termed transcription, hence the alternative term "direct transcription" for direct collocation. In this approach, direct orthogonal local collocation with barycentric Lagrange interpolation[36] is employed. This method represents the most effective approach for storing and assessing high-order orthogonal polynomials.

This is achieved by expressing the value of the function at any point $f(t)$ using a weighted combination of the function's value $f_i = f(t_i)$ at the roots of the orthogonal polynomial t_i. The equation for barycentric interpolation is provided below. It's worth noting that this expression is invalid when evaluated at the interpolation points $t = t_i$. However, this presents no issue as the function value at these points is already known to be f_i.

$$f(t) = \frac{\sum_{i=0}^{n} \frac{v_i}{t-t_i} f_i}{\sum_{i=0}^{n} \frac{v_i}{t-t_i}} \tag{4.16}$$

where the interpolation weights v_i are calculated by

$$v_i = \frac{1}{\prod_{j=0, j\neq i}^{n} (t_i - t_j)}, \quad i = 0, \dots, n \tag{4.17}$$

The barycentric interpolation formula (4.16) will still interpolate the data at points f_i if the weights v_i are chosen arbitrarily. The choice of weights given by (4.17) is special in that it defines the unique polynomial interpolant, whereas any other choice of weights will result in interpolation by some rational function [36]. Notice that these weights can be scaled by an arbitrary constant and still produce the correct interpolation in Equation (4.16).

Barycentric interpolation would be used to assess the solution in an orthogonal collocation method. However, it is not employed in the construction of the nonlinear program; rather, the decision variables of the nonlinear program are the values of the state and control at each collocation point t_i.

Firstly, the total length of the track (the independent variable) is divided into N finite elements (hence N + 1 grid points, denoted as s_k) of arbitrary length ds_k. The states within each interval are approximated by a Legendre polynomial of degree d, with the collocation points $s_{k,j}$ selected as the roots of the Legendre polynomials. These roots are typically defined in the interval $[-1, 1]$, but they can be mapped to any other interval by uniformly scaling the points. In addition to the previously mentioned benefits, this selection of collocation sites yields the best accurate estimate of the related quadrature formula.

$$k = \{1, \dots, N+1\}$$

$$j = \{1, \dots, d\}$$

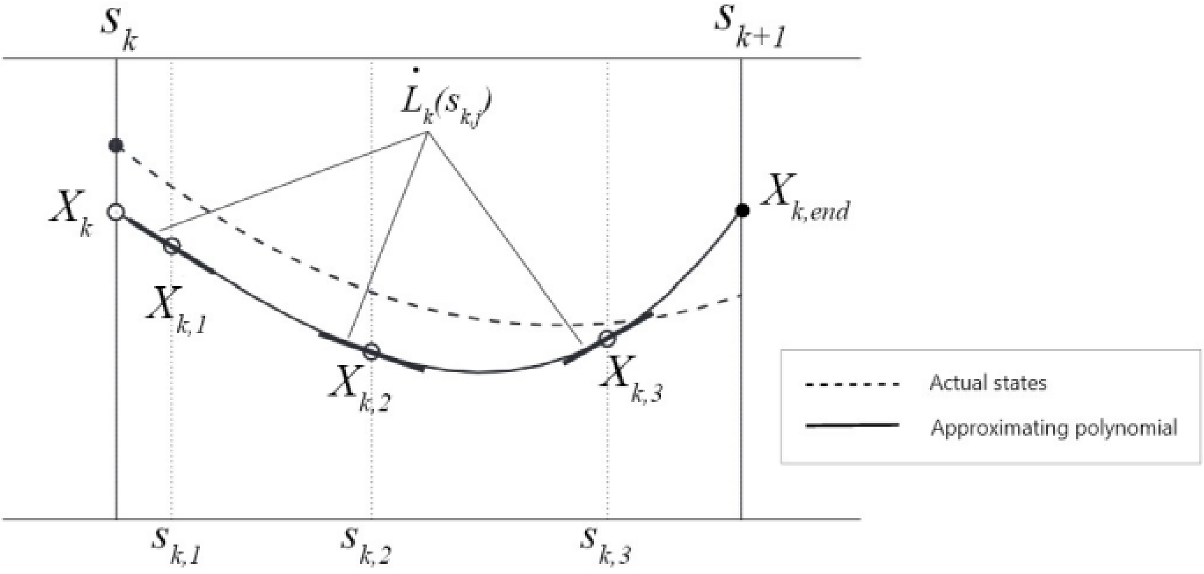

Figure 4.1: Discretisation Interval

The approximating polynomial shown in Figure 4.1 does not yet satisfy the collocation constraints. $X_{k,j}$ represents the auxiliary states used to formulate these constraints by evaluating the system dynamics at those points. $\dot{L}_k(s_{k,j})$ denotes the derivative of the polynomial at the collocation points.

Another advantage of employing orthogonal polynomials with barycentric Lagrange interpolation is the ability to compute differentiation, integration, and interpolation of the polynomials as a linear combination of their values at the collocation points. This linear combination involves the decision variables of the NLP. For example, consider defining $\mathbf{L}_k = [l_k(s_{k,1}), l_k(s_{k,2}), \ldots, l_k(s_{k,d})]$, where $l_k(s)$ represents the Lagrange polynomial of order d in the interval $[s_k, s_{k+1}]$, and $s_{k,j}$ represents the collocation points. It should be noted that $l_k(s_{k,j}) = X_{k,j}$. Consequently, the derivatives at the collocation points can be determined as follows:

$$\dot{\mathbf{L}}_k = \frac{\mathbf{C}}{dsk} \cdot \mathbf{L}_k \tag{4.18}$$

The same approach can be used to determine the contribution of each finite element to the objective function, denoted as $\mathbf{Sf}_k = [S_f(sk,1), S_f(sk,2), ..., S_f(sk,d)]$; and to extrapolate the state at the end of the interval. Matrices $\mathbf{C}$, $\mathbf{B}$, and $\mathbf{D}$ can be computed for a 'standardized' interval like $[0,1]$, and their structure and values would solely depend on the chosen degree for the polynomial.

$$J_k = \mathbf{B} \cdot \mathbf{Sf}_k \cdot dsk \tag{4.19}$$

$$X_{\text{end}} = \mathbf{D} \cdot [X_k, X_{k,1}, \ldots, X_{k,d}] \tag{4.20}$$

The derivatives of the polynomials are matched with the system's real dynamics at the collocation locations, and the extrapolated final state of each finite element is matched with the first state of the subsequent one to create the collocation constraints.

Normally, the control inputs are discretized as piece-wise constant functions, but in this case, linear functions are employed. This is accomplished by specifying the input values at the grid points rather than the intervals, thereby increasing the number of decision variables only by the number of inputs. This approach often leads to faster solution times. Additionally, path constraints can be formulated more directly since they can now be defined at every grid point. Moreover, it facilitates the computation of derivatives in each interval for applying constraints on the input rates. The same principle is applied to discretize the auxiliary variables y.

At last, the NLP formulation yields the following results:

minimize

$$J = \sum_{k=1}^{N} \mathbf{B} \cdot \mathbf{Sf}_k \cdot d_{s_k} \tag{4.21}$$

subject to

$$\frac{d}{ds} L_k(s_{k,j}) - \mathbf{f}(X_{k,j}, U_k, Y_k, p, \kappa_k) = 0 \quad \forall k \in [0, N] \text{ and } j \in [1, d] \tag{4.22}$$

$$X_{end} - X_k = 0 \quad \forall k \in [1, N+1] \tag{4.23}$$

$$\mathbf{H}_{lb} \leq h(X_k, U_k, Y_k, p, \kappa) \leq \mathbf{H}_{ub} \quad \forall k \in [0, N] \tag{4.24}$$

$$\mathbf{B}_{lb,k} \leq h(X_k, U_k, Y_k, p, \kappa) \leq \mathbf{B}_{ub,k} \quad k = 0,\, k = N + 1 \tag{4.25}$$

The conversion involves transforming the objective function 4.11(32) into 4.21, the system's dynamic constraints 4.12 into the collocation constraints 4.22 and 4.23, the path constraints 4.13 become 4.24, and the boundary constraints 4.14 appear as 4.25. Path (and boundary) constraints can be treated as equality constraints by setting $H_{\text{lb}} = H_{\text{ub}}$; however, implementing them as equality constraints is facilitated by allowing a slight slack. This approach has been observed to reduce simulation times. The decision variables are then modified as follows:

states	X_k
helper states	X_{kj}
inputs	U_k
auxiliary variables	Y_k
parameters	p

The "decision space" is lowered since each decision variable is subject to constant boundaries. This process limits the inputs' lowest and maximum values as well as certain states, such as the maximum speed based on the maximum power and drive torque or the maximum distance to the center line, which, as previously said, ensures the car stays on the track. As seen in 4.10, the NLP incorporates an extra set of restrictions to restrict the maximum rate of change of the inputs. The inputs' derivative is computed as:

$$\Delta U_k = \frac{U_{k+1} - U_k}{d_{sk}} \tag{4.26}$$

4.3 State and Control Scaling

Scaling plays a crucial role in determining the efficiency of optimization algorithms. As convergence criteria rely on defining what constitutes "small" and "large" values, problems arising from irregular or unbalanced scaling can pose challenges. One approach to scaling involves transforming variables from their original form, often reflecting the physical aspects of the problem, into variables that exhibit more favourable characteristics for optimization purposes.

4.3.1 Non-Dimensionalisation

In problems involving physical quantities, inadequate scaling can often stem from the choice of problem units. In our scenario, adopting SI units results in the vehicle's main frame having a mass of around 860 kg including driver, and the acceleration due to gravity is approximately $9.8\,\mathrm{m/s^2}$. When considering the impact of aerodynamic downforce, normal tire loads and tire friction forces can reach magnitudes on the order of 10^4 N in certain situations. Consequently, forces exerted on the vehicle are approximately four orders of magnitude greater than length-related variables, angles (such as steering), and tire slip coefficients. To address this issue, we normalize the fundamental physical units of length, mass, and time, making all mass- and length-related parameters unitless, while ensuring that the vehicle possesses unit mass and unit length. Additionally, time is adjusted so that the acceleration due to gravity becomes unity. Following non-dimensionalization, angles remain expressed in radians.

In situations where the maximum value of certain variables is known, scaling is achieved by dividing these variables by their respective maximum values. For instance, the decision variables associated with the drive torque are divided by the maximum drive torque, which is a parameter defined in the car model. However, the objective function remains unscaled, as scaling it was found to diminish the solver's performance, although other studies have reported benefits from scaling the objective function. Similarly, the path constraints are scaled to ensure that the magnitude of h remains comparable to that of the decision variables. Nonetheless, conducting a comprehensive investigation into the effects of scaling could prove highly valuable in this context.

4.4 Regularisation

The existence of singular arcs in an OCP might cause solution oscillations and convergence issues. This phenomenon arises when there are several solution sets, and distinct sets of choice variable values provide equal (or extremely similar) objective function values. Regularization is a strategy for favouring specific solutions by inserting penalty terms.

Typically, these terms are corrected with a regularization factor. Choosing sufficiently small values ensures that the objective function is closely aligned with the original. Squaring the inputs is one of the most basic regularization terms, to reduce control effort, a typical difficulty in fields such as robotics.

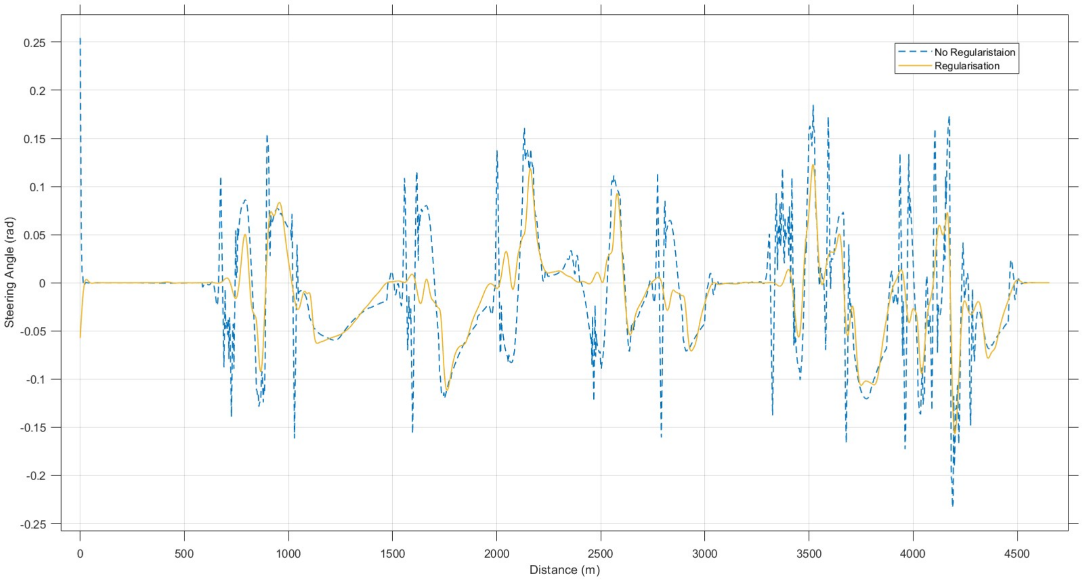

Figure 4.2: Steering angle with and without applying regularisation

An advanced technique penalizes solutions that lack smoothness by including input derivatives. To address solutions with oscillations, the second derivative is also included. Regularization is not restricted to inputs; it also applies to auxiliary variables Y_k. After integrating the regularization terms, the objective function changes to:

$$J = \sum_{k=1}^{N} \left[\mathbf{B} \cdot \mathbf{Sf}_k \cdot ds_k + r_u \cdot Uk^2 + r_{du} \cdot \Delta Uk^2 + r_{du2} \cdot \Delta^2 U_k^2 + r_{dy} \cdot \Delta Yk^2 + r_{dy2} \cdot \Delta^2 Y_k^2 \right] \quad (4.27)$$

where $U_k = [T_{drv,k}, T_{brk,k}, T_{regen,k}, \delta_k]$ and $Y_k = \Gamma_{x,k}$. The regularization factors were chosen as follows:

$$
\begin{aligned}
r_u &= [0,\ 0,\ 0,\ 0.1] \\
r_{du} &= [0.01,\ 0.01,\ 0.01,\ 0.1] \\
r_{du2} &= [0.01,\ 0.01,\ 0.01,\ 10] \\
r_{dy} &= 0.001 \\
r_{dy2} &= 0.015
\end{aligned}
$$

4.5 Initial guess

The NLP solver relies on an iterative approach, which necessitates an initial estimation of the decision variables. While a straightforward initialization, such as a linear interpolation between the initial and final states, suffices for certain problems, more intricate systems typically demand a more informed initial estimate.

In situations where locating initial guesses proves challenging, a common strategy involves resolving a simplified rendition of the problem and then incorporating the solution into the complete problem. This technique may include several intermediary steps before reaching the final solution.

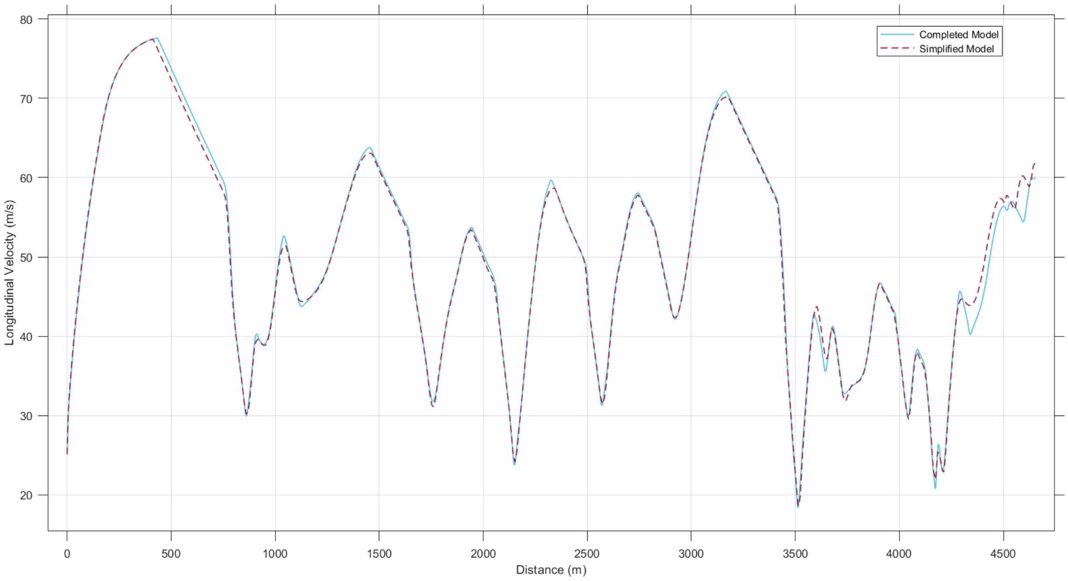

Figure 4.3: Comparison of the longitudinal velocity with a simplified model and the complete model

In this study, a brief examination was conducted on a particular concept. The problem was made easier by excluding wheel dynamics, load transfer considerations, and utilizing linear tires. Employing this simplified setup, along with a collocation step of 10 meters, facilitated the discovery of optimal inputs and states within a time frame of under 207 seconds. Conversely, employing the complete model, which utilizes a step size of 3 meters, required approximately 2952.7 seconds.

The solutions from the fast and final problems may appear similar on a variable-by-variable basis as shown if Figure 4.3 and 4.4, the combination of values obtained in the 'fast' problem might not be viable for the complete problem. Furthermore, the initial guess, despite being closer to the optimal solution, might be situated in regions of the objective function space where an NLP solver like ipopt struggles to converge towards the optimal solution.

Finally, the chosen strategy involved setting all decision variables to'reasonable' constant values.

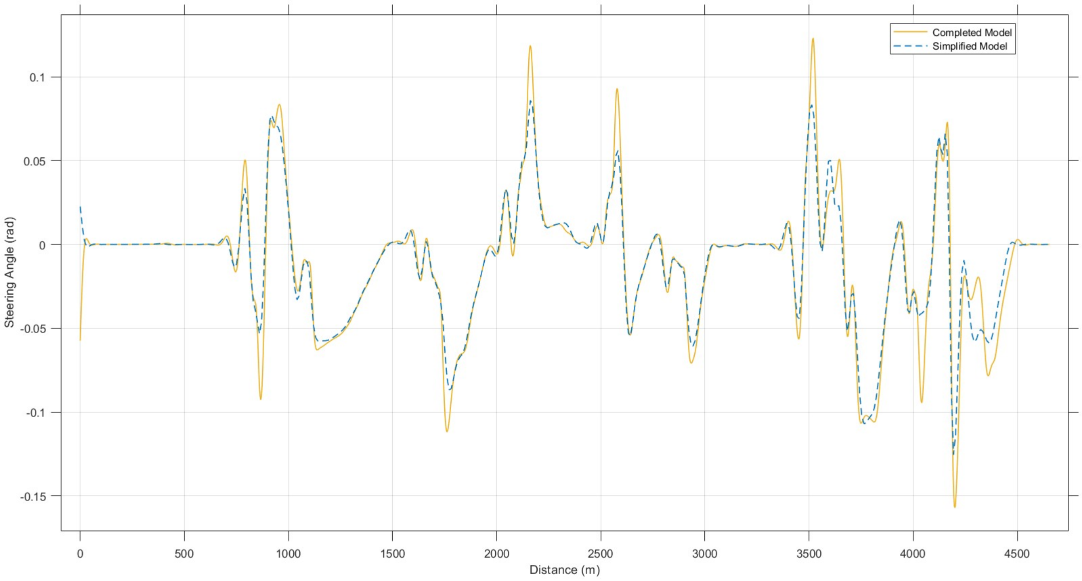

Figure 4.4: Comparison of the steering angle with a simplified model and the complete model

For example, picking a number for the longitudinal velocity that is closely related to the final solution's average speed resulted in faster simulation durations. Similarly, aligning the wheels' rotational speed with the vehicle's longitudinal speed improved the solver's performance.

Chapter 5

Simulation Results and Discussion

This section presents the simulation results and their analysis. Initially, it delves into the intricacies of discovering the optimal race line and controls for the Barcelona circuit, ensuring that the derived solutions align with anticipated behaviours. Following this, a comprehensive optimization study is undertaken for the Formula E car, specifically examining its performance during a race scenario without activating the attack mode. Subsequently, the analysis extends to explore the advantages gained from employing the attack mode, shedding light on its impact on overall performance. In addition, the effect of the energy consumption limits on the vehicle's performance is studied. Through these varied scenarios, the section provides insightful demonstrations of the software's effectiveness in addressing real-world challenges within the world of racing simulations.

5.1 Race Line Optimisation

The MLTP aims to discover the best control settings. This is tested out on the Barcelona Circuit. By looking at Figure 5.3, it's evident that the car sticks to the centre of the track during the race, resulting in a longer lap time. However, the goal is to rectify this and ensure the car achieves the shortest lap time possible with the best racing line.

The chosen circuit is the Circuit de Barcelona-Catalunya, spanning 4.654 kilometres (2.891 miles) in Montmeló, Barcelona, Catalonia, Spain. Renowned for its lengthy straights and diverse array of corners, this circuit is hailed as a versatile racing track. Additionally, the Circuit de Barcelona-Catalunya holds an esteemed FIA Grade 1 license. Although this circuit does not host Formula E races, it was chosen for this study since no data on Formula E circuits was available.

Once the optimization process is complete for the track, it becomes evident that there have been significant improvements in the race line, as depicted in Figure 5.4. Particularly noticeable enhancements occur during the corners within the first and third sectors. We observe the car smoothly adhering to the optimized race line, particularly evident from turn 1 to turn 4 in the first sector, and from turn 10 to turn 16 in the third sector. These adjustments contribute to initiating the lap with the most efficient trajectory from the very outset, leading to minimized lap times.

Figure 5.1: The Circuit de Barcelona-Catalunya [37]

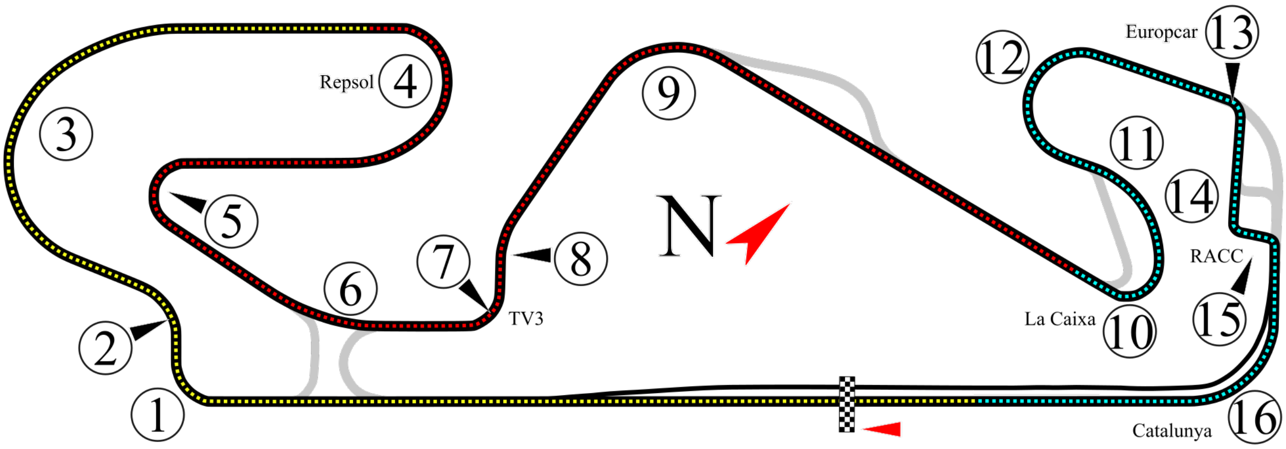

Figure 5.2: Track map layout [38]

5.2 Simulation set-up

This section offers an overview of the vehicle and powertrain parameters, as well as the state and control variables utilized in the vehicle model. These parameters and variables are incorporated into Casadi to solve the NLP within Matlab.

Table 5.1 displays the vehicle parameters utilized in this simulation. The vehicle model comprises 10 state variables, each with its respective scaling, as depicted in Table 5.2.

In this simulation, consistent values were employed for maximum driving, braking, and regenerative torques, as well as for brake balance and the proportion of regenerative brake in total brake torque, both with and without attack mode. The only disparity lies in the maximum power output, which increased by 50 kWh during attack mode, elevating from 300 kWh to 350 kWh.

Table 5.1: Vehicle Parameters

Symbol	Description	Value
M	vehicle mass [kg]	856
Iz	moment of inertia about the z-axis [kg m^2]	450
w	wheelbase [m]	2.97
a	distance of the mass center from the front axle [m]	1.44
b	distance of the mass center from the rear axle [m]	$w - a$
h	height of center of gravity [m]	0.3
D_{roll}	roll moment distribution (fraction at the front axle)	0.5
w	wheel to car centerline distance [m]	0.73
R_f	front wheel radius [m]	0.33
R_r	rear wheel radius [m]	0.33
k_d	differential friction coefficient [Nms/rad]	10.47
C_d	drag coefficient	0.57
C_l	downforce coefficient	1.5
A	frontal area [m^2]	1.5
ρ	air density [kg/m^3]	1.2
a_A	center of pressure to front axle distance [m]	1.2
b_A	center of pressure to rear axle distance [m]	$w - a_A$

Table 5.2: State Variables

Symbol	Description	Scale
vx	longitudinal velocity [m/s]	100
vy	lateral velocity [m/s]	10
$\dot{\psi}$	yaw rate [rad/s]	1
n	lateral position to centreline [m]	5
ψ	angle to centreline tangent direction [rad]	1
w_1	angular velocity front left tyre [rad/s]	$\frac{vx_s}{R_f}$
w_2	angular velocity front right tyre [rad/s]	$\frac{vx_s}{R_f}$
w_3	angular velocity rear right tyre [rad/s]	$\frac{vx_s}{R_r}$
w_4	angular velocity rear left tyre [rad/s]	$\frac{vx_s}{R_r}$
$Elap$	Energy consumption [J]	52*3.6e6

Table 5.3: State limits

States	Lower limit	Upper limit
vx [m/s]	1e-3	$v_{maximum}$
vy [m/s]	-10	10
$\dot{\psi}$ [rad/s]	-$\frac{\pi}{2}$	$\frac{\pi}{2}$
n [m]	-4	4
ψ [rad]	-$\frac{\pi}{4}$	$\frac{\pi}{4}$
w_1 [rad/s]	0	$\frac{v_{max}}{Rw_F}$
w_2 [rad/s]	0	$\frac{v_{max}}{Rw_F}$
w_3 [rad/s]	0	$\frac{v_{max}}{Rw_R}$
w_4 [rad/s]	0	$\frac{v_{max}}{Rw_R}$
Elap during Race Mode [kWh]	0	1.6
Elap during Attack Mode [kWh]	0	2.16

Table 5.4: Powetrain Parameters

Symbol	Description	value
$Tdrive_{max}$	maximum driving torque [Nm]	2000
$Tbrake_{max}$	maximum braking torque [Nm]	6000
$Tregen_{max}$	maxmum Regenrative torque [Nm]	2000
P_{max}	maximum driving power without attack mode [kWh]	300
P_{max}	maximum driving power with attack mode [kWh]	350

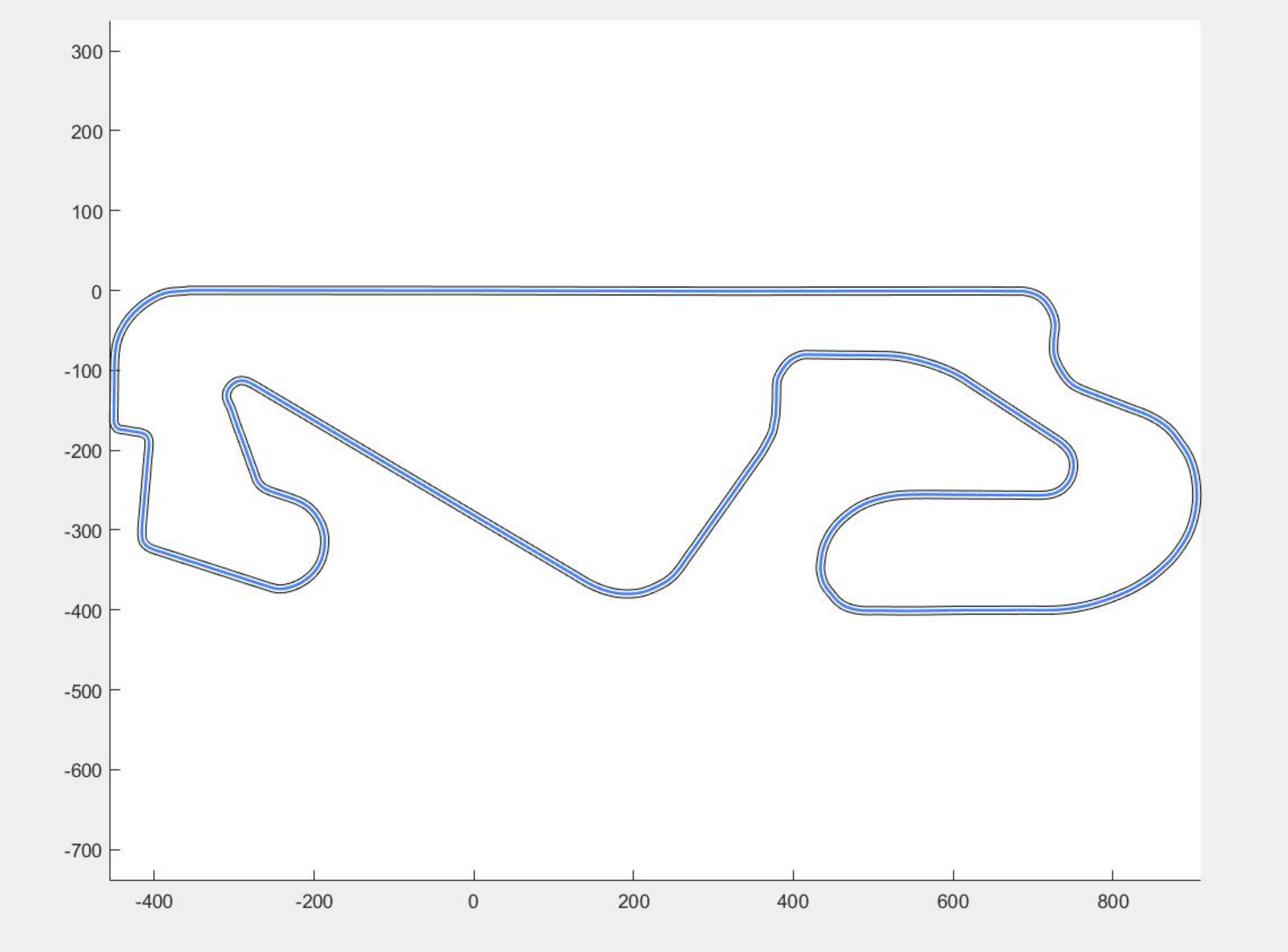

Figure 5.3: 2D Plot of Barcelona Circuit

Table 5.5 displays the four control variables utilized in the simulation, along with their respective scaling factors.

Table 5.5: Control Variables

Symbol	Description	Scale
$Tdrive$	driving torque [Nm]	$Tdrive_{max}$
$Tbrake$	braking torque [Nm]	$Tbrake_{max}$
$Tregen$	Regenrative torque [Nm]	$Tregen_{max}$
$delta$	steer angle [rad]	$\frac{\pi}{8}$

Table 5.6: Control limits

Control variables	Lower limit	Upper limit
Tdrive	0	2000
Tbrake	-12000	0
Tregen	800	0
delta	-$\frac{\pi}{4}$	$\frac{\pi}{4}$

Several key definitions were established for the optimization problem and collocation method. Boundary conditions for the state variables were defined, with all initial and final states set to NaN except for the initial velocity, which was fixed at 25 m/s. Additionally, the collocation

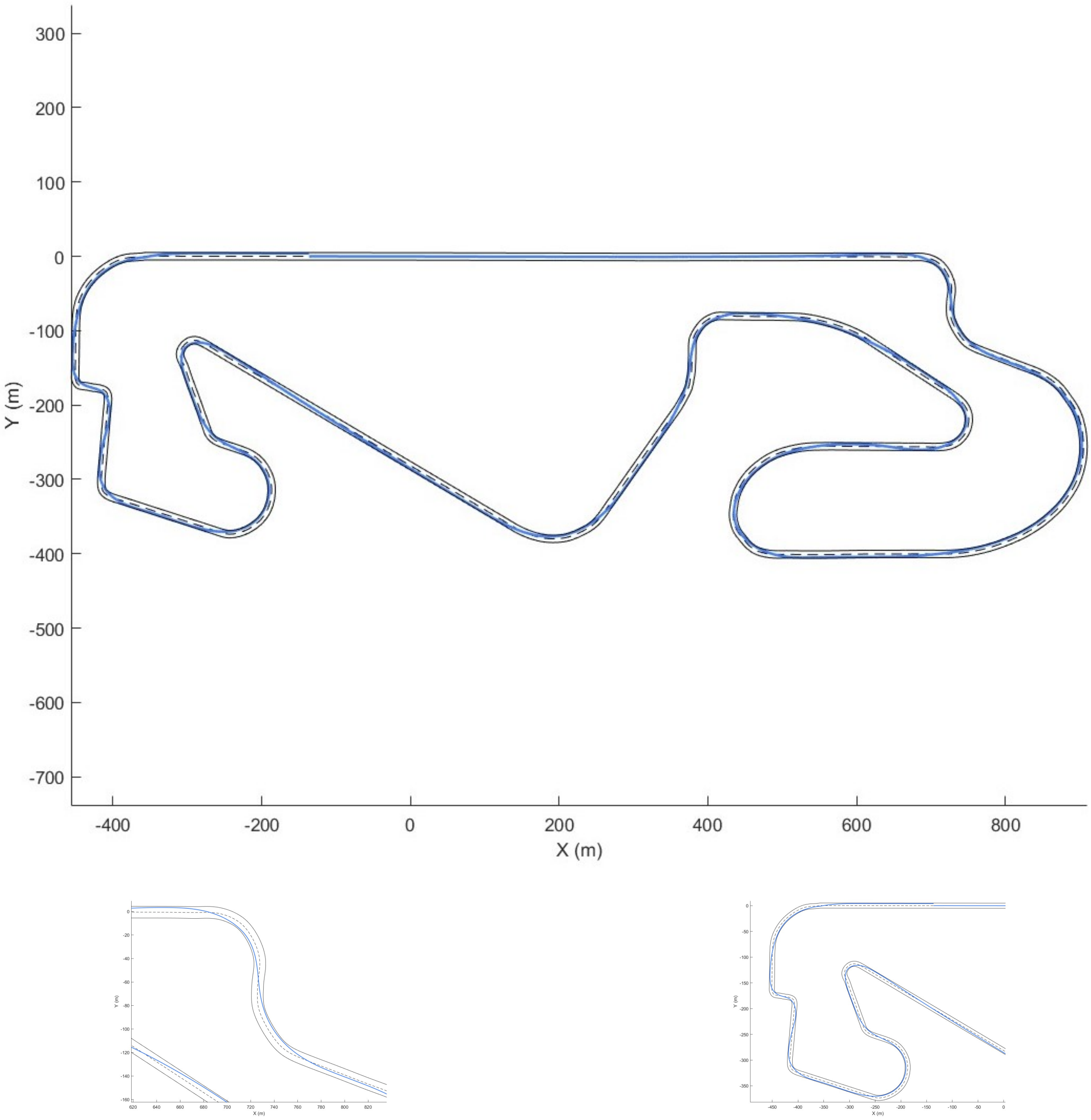

Figure 5.4: Optimal race line of Barcelona Circuit

Table 5.7: Path Constraints

Constraints	Lower limit	Upper limit
Brake and throttle overlap	-1e-3	1e-3
Regenerative brake and throttle overlap	-1e-3	1e-3
Longitudinal load transfer	-1e-3	1e-3
mu_1	0	Infinite
mu_2	0	Infinite
mu_3	0	Infinite
mu_4	0	Infinite

step was set to 3 m with 3 degrees of interpolating polynomials. The simulation ran for 1000 iterations.

Furthermore, the control variables' rate of change was constrained. These limitations are critical in ensuring that changes in the input variables throughout the simulation do not occur too quickly, preventing the system from becoming unstable or unrealistic. The limits are:

upper bounds = [10000, 10000, 10000, 1]
lower bounds = [-10000, -10000, -10000, 1]

5.3 Race Mode

In this section, the performance of the Formula E car during the race will be demonstrated, highlighting the results obtained following the implementation of optimized control techniques.

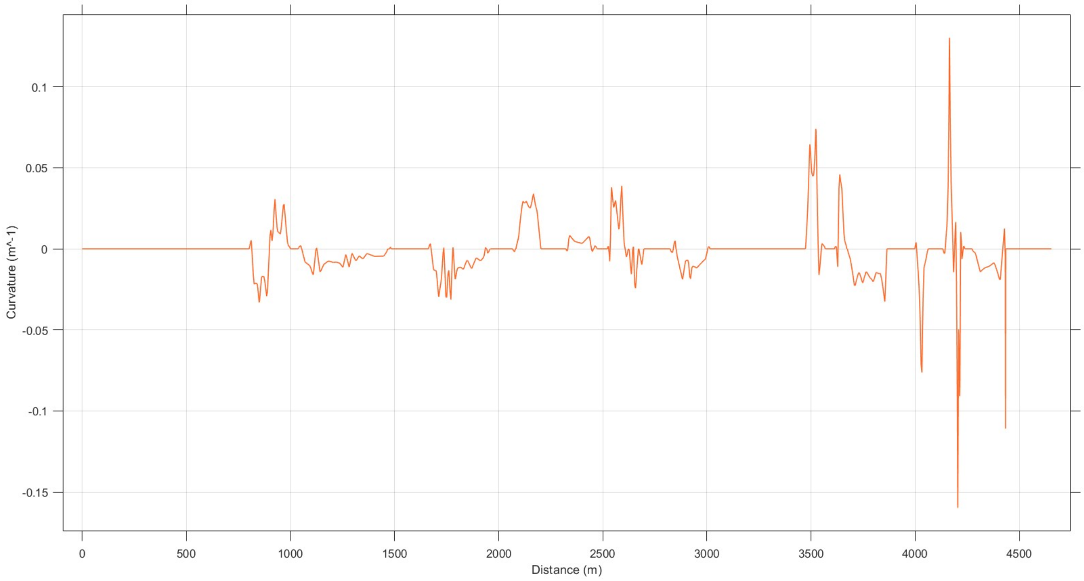

Figure 5.5: Curvature

The positive and negative values of the segment radius of curvature differentiate the left and right curves. The segment curvature is found by:

$$C = \frac{1}{R} \tag{5.1}$$

The input data is reorganized and used in equation (3.12). The total length of the track centre line is 4654 meters, with the vehicle's initial velocity set at 25 m/s. The initial position of the car's centre of mass is situated at the starting point of the track, precisely at coordinates x = -136.35 and y = -0.04. The elapsed time of the simulation is 2952.7 seconds, enabling the vehicle to complete a single lap of the circuit in 96.338 seconds.

Figure 5.6 illustrates the relationship between the steering angle and distance across the entire lap, providing insights into the results and their correlation with the curvature of the track. The findings demonstrate the controller's effectiveness in adjusting the steering angle to accommodate changes in curvature. When the trajectory exhibits positive curvature, indicating a left turn, the steering angle aligns accordingly, directing the wheels to the left and facilitating smooth navigation along the curvature of the road. Conversely, in instances of negative curvature, indicative of right turns, the steering angle adjusts in the opposite direction, steering the wheels to the right, thereby enabling the vehicle to negotiate left turns with the requisite curvature. Furthermore, an examination of Figure 5.5 allows for a straightforward comparison between

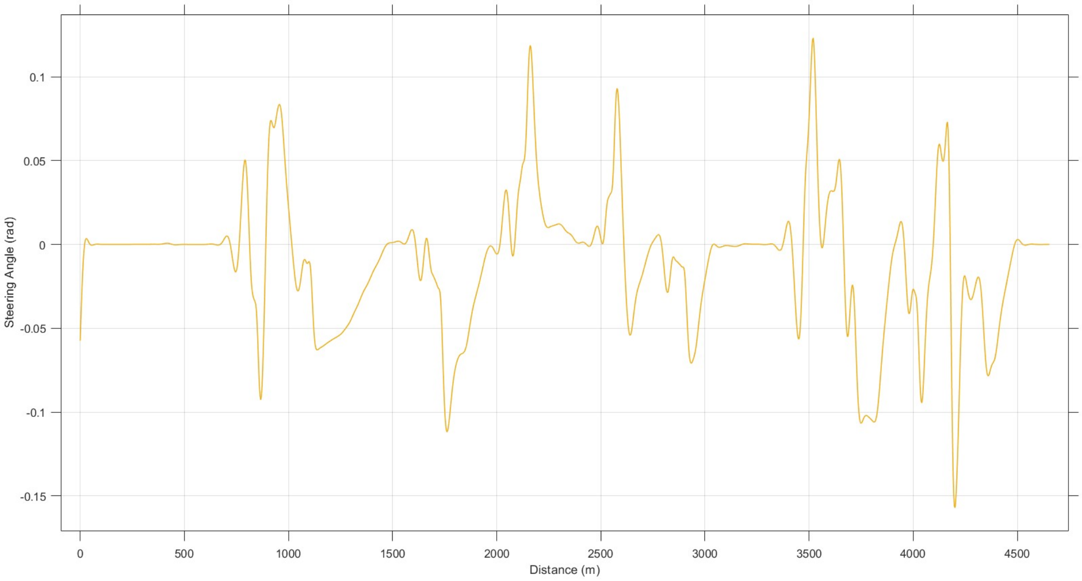

Figure 5.6: Steering angle during the entire lap

the variations in steering angle and the corresponding changes in track curvature, providing a comprehensive understanding of the controller's performance throughout the lap.

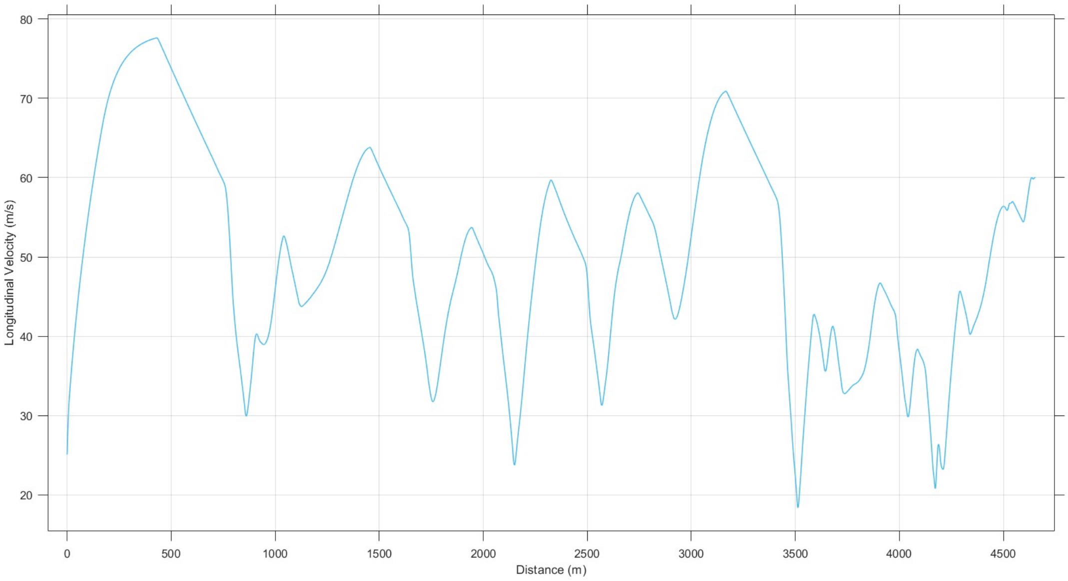

Figure 5.7: Longitudinal velocity

The longitudinal velocity of a Formula E car refers to its speed along the direction of its motion. This velocity represents the rate of change of the car's position along the track, indicating how fast it is accelerating or decelerating in a straight line. During the race mode, a maximum power of 300 kWh can be used by each driver, and as it is shown in Figure 5.7 it is possible to see that the results of the longitudinal velocity were satisfied where it achieved a maximum speed of 77.6 m/s (279.36 km/h) which is reasonable since the maximum speed that can be achieved is around 88.88 m/s (320 km/h) [5].

However, there is a difference of approximately 10 m/s this might be due to several reasons. In Formula E racing, the attainment of maximum speeds during races is influenced by various factors. These include the need for energy conservation due to battery limitations, regulatory restrictions on power output, the challenging layout of street circuits featuring tight corners, the aerodynamic design focused on efficiency rather than top speed, and strategic considerations such as energy management by drivers. These factors collectively impact the ability of Formula E cars to consistently reach their highest speeds during races.

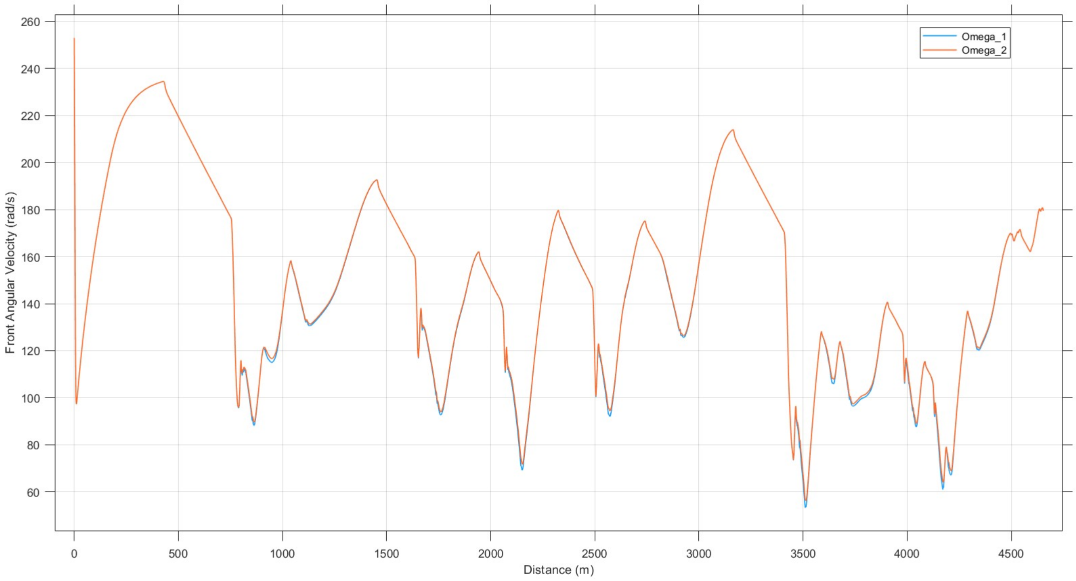

Figure 5.8: Front angular velocity

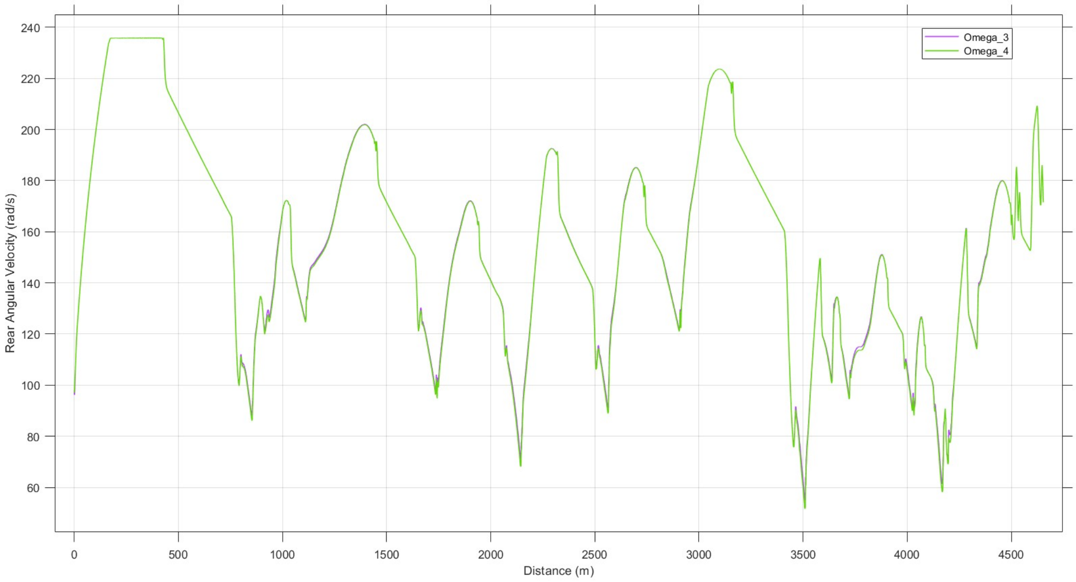

Figure 5.9: Rear angular velocity

Furthermore, the wheel motion of the tyres which was mentioned in equations 3.36, 3.37, 3.38, 3.39 pertains to the dynamic movement and rotation of the wheels of a Formula E car as it traverses the track. This motion directly influences the longitudinal velocity. In the analysis, the angular velocity of the front wheels is depicted in Figure 5.8, while that of the rear wheels is illustrated in Figure 5.9. Given that Formula E cars have a rear-wheel drive configuration, it can be seen from Figure 5.9 that the longitudinal velocity is dependent on the angular velocity of the rear wheels. Notably, the angular velocity exhibits limitations and fails to achieve its peak values during specific intervals, namely between distances 0-750 m, 1400-1600 m, 2300-2400 m, and 3100-3300 m. These limitations are attributed to the absence of team-specific data, which hinders a more comprehensive analysis.

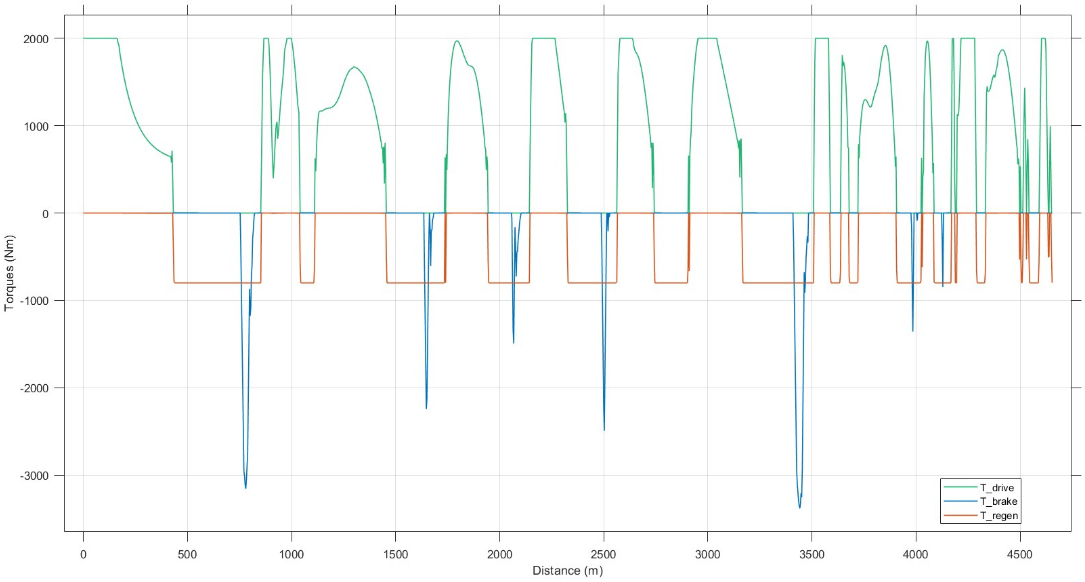

Figure 5.10: Drive, brake and regenerative pedal torques

Figure 5.10 displays the dynamics of the driving, braking, and regenerative torques throughout the lap. At the beginning of the lap, the driver applies full throttle due to the initial straight line, covering a distance of approximately 700 meters before encountering the first corner at turn 1 in the first sector. However, the car cannot maintain maximum driving torque throughout the straight line due to power limitations, which hinder its ability to reach its top speed of 320 km/h. Towards the end of the line, the car reaches its highest speed of the lap. Hence, the driver has to apply significant braking force to make the first corner. Consequently, the regenerative torque reaches its limit in the first sector.

From turn 2 until the end of sector 1 before turn 4, the driver again applies full throttle due to the high-speed cornering. However, the car does not reach the speed achieved at the end of the initial straight. Despite this, the driver achieves the second-highest regenerative torque on the lap, as turn 1 necessitates more braking than turn 4.

Following turn 4, the driver maximizes throttle input until turn 5, as well as during the exit from turn 7 until turn 9, owing to the shorter distances between corners compared to previous sections. However, similarly to the initial straight, the car cannot sustain maximum torque levels throughout the straight between turns 9 and 10 due to power limitations.

After turn 10, the driving torque reaches its peak, facilitated by the shorter distances between subsequent turns. The regenerative torque registers its limit for the shortest distance due to the proximity of the corners until turn 15 which leads to lower speeds than the earlier sectors. Finally, the driver applies full throttle until the end of the lap, yet the car remains unable to maintain maximum driving torque until the end.

Overall, torque dynamics vary based on the track's features, but the car is unable to sustain maximum torque output throughout the longer straights. This is due to the power limitations which prevent the car from reaching its top speed. Furthermore, the vehicle maintains the maximum regenerative torque for the longest distance at the end of the straights where the highest speeds are reached, due to increased braking requirements.

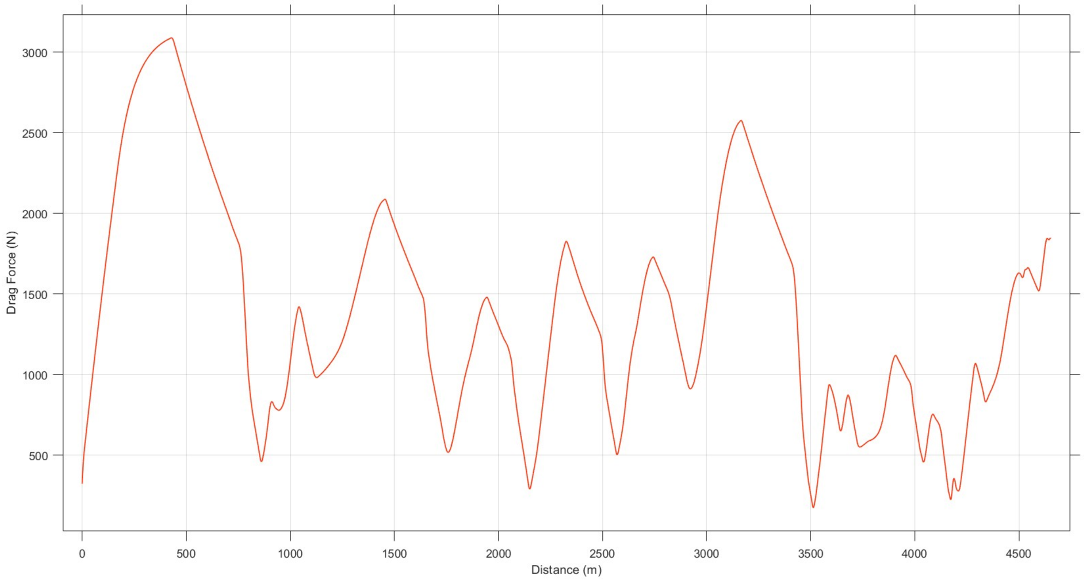

Figure 5.11: Drag Force

Figure 5.11 illustrates the variation of drag force throughout the entire lap. The shape of the drag force curve closely mirrors the longitudinal speed of the car. This correlation arises from the dependence of the drag force on the square of the longitudinal speed, as illustrated in equation 3.52.

The data presented in the figure reveals that the drag force peaks between the starting line and turn 1, as well as between turn 9 and turn 10, where there are long straight sections of the track. In these areas, the car encounters maximum aerodynamic resistance, due to the achieved high speeds on those straights.

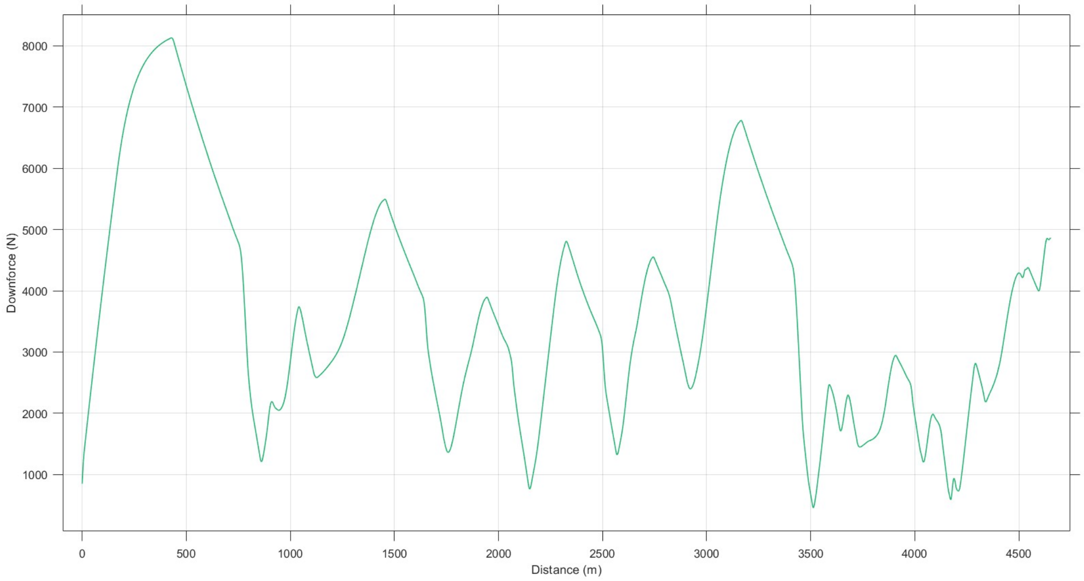

Figure 5.12: Downforce

Figure 5.12 demonstrates the trend of the downforce throughout the lap. This force is crucial for how well Formula E cars perform and handle on the track. Unlike road cars, which try to reduce lift to save fuel and stay stable, Formula E cars depend on aerodynamic downforce to improve grip during cornering and overall track performance.

The graph shows that the downforce, produced mainly by the front and rear wings, increases as the car goes faster, reaching its highest point at the initial straight where the car reaches its top speed. This downforce pushes the car down onto the track, making it stick to the road better. This relationship between downforce and air resistance, shown in 3.51, is crucial for engineers to balance when designing Formula E cars for maximum speed and efficiency on the track.

Figure 5.13 depicts the energy consumption profile of the car throughout the lap. Noticeably, the highest consumption occurs along the extended initial straight, preceding the first corner. Subsequently, the car regenerates energy, enabling it to complete the lap while adhering to the maximum energy consumption limit of 5.76e03 kJ (1.6 kWh). Moreover, elevated energy consumption is observed in the first and second sectors, with heightened regeneration occurring, particularly during the fast corner at turn 3 and the straight stretch between turns 9 and 10. The fast sections entail increased energy consumption, thereby allowing for more significant regeneration.

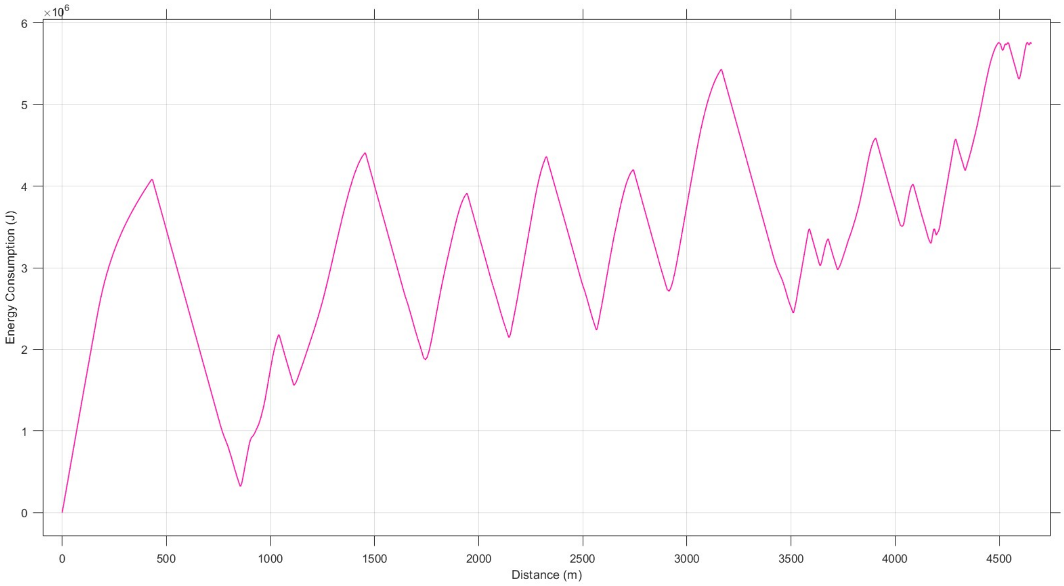

Figure 5.13: Energy consumption

Figure 5.14 displays the variation in slip angles during racing mode, while Figure 5.15 depicts the lateral velocity. Additionally, Figure 5.16 illustrates the slip ratios of the tyres. Furthermore, Figures 5.17, 5.18, and 5.19 represent the longitudinal, lateral, and vertical tyre forces, respectively. Finally, Figure 5.20 provides insights into auxiliary load transfers.

5.4 Attack Mode Activation

Figure 5.21 illustrates the effect of Attack Mode on the longitudinal velocity. The graph indicates that during Attack Mode, the car is capable of achieving a higher maximum speed compared to when Attack Mode is not activated. This difference is particularly noticeable at the start of the lap, where there is a lengthy straight section, as well as during the high-speed corner at turn 3 and the subsequent straight stretch from turn 9 to turn 10.

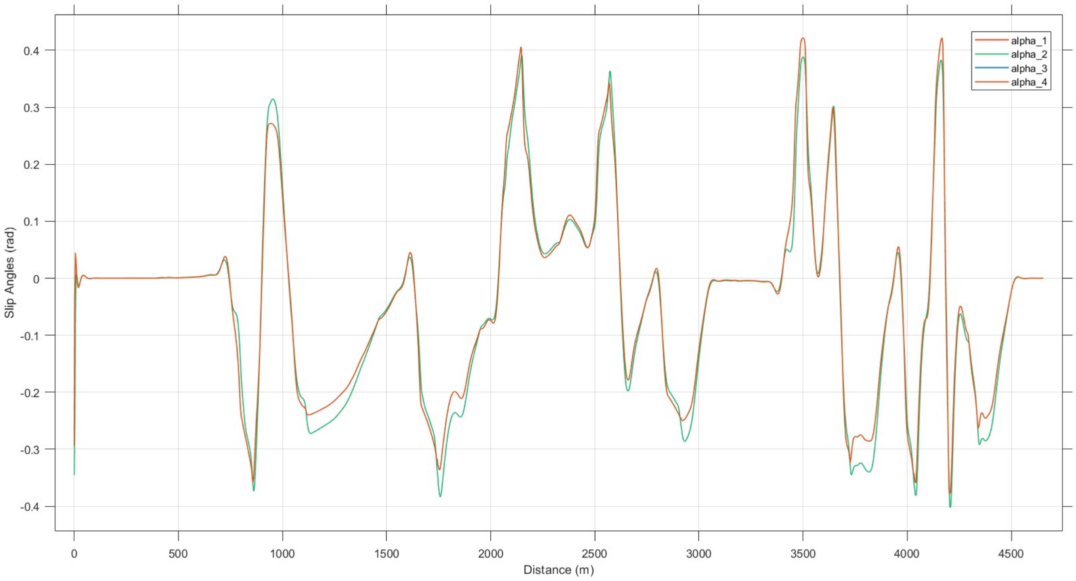

Figure 5.14: Slip Angles

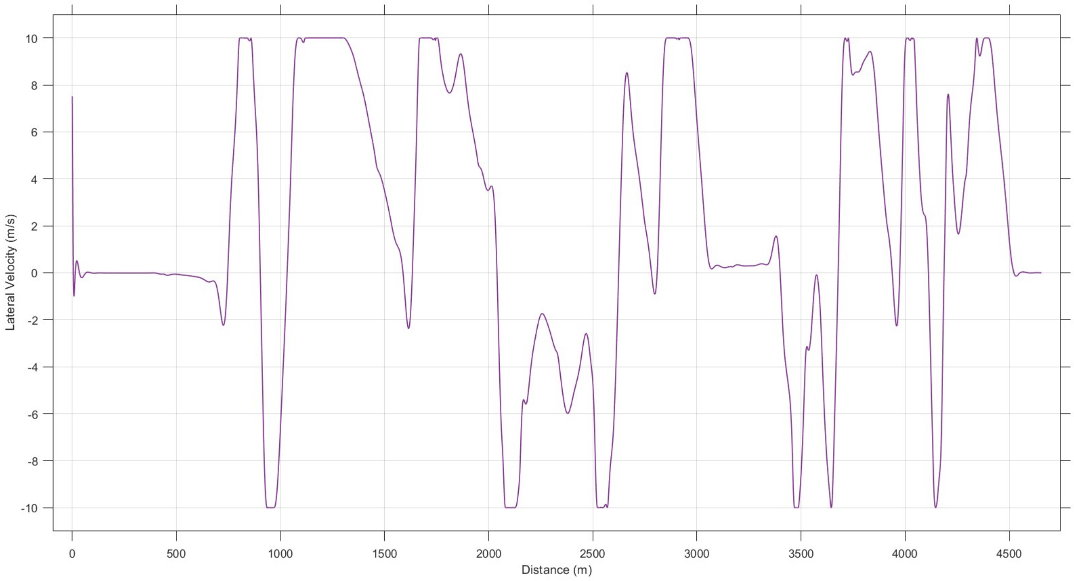

Figure 5.15: Lateral velocity

Conversely, during slow corners and in the short distances leading up to turns, the longitudinal speed of the car remains unchanged whether Attack Mode is activated or not. This suggests that while Attack Mode provides a speed advantage in certain sections of the track, it does not significantly affect the car's speed in slower or more technical parts of the circuit.

Figure 5.22 illustrates the variance in driving torque between the activation and deactivation of Attack Mode. It is evident from the graph that the driving torque experiences enhancement, particularly noticeable in the first and second sectors, attributable to the power boost provided by Attack Mode. However, despite this power increase, the car is not able to maintain maximum driving torque throughout the entirety of certain sections, namely before the first turn and the straight line between turns 9 and 10. Notably, the lap done in this simulation after the lap where the driver change the racing line to activate the attack mode.

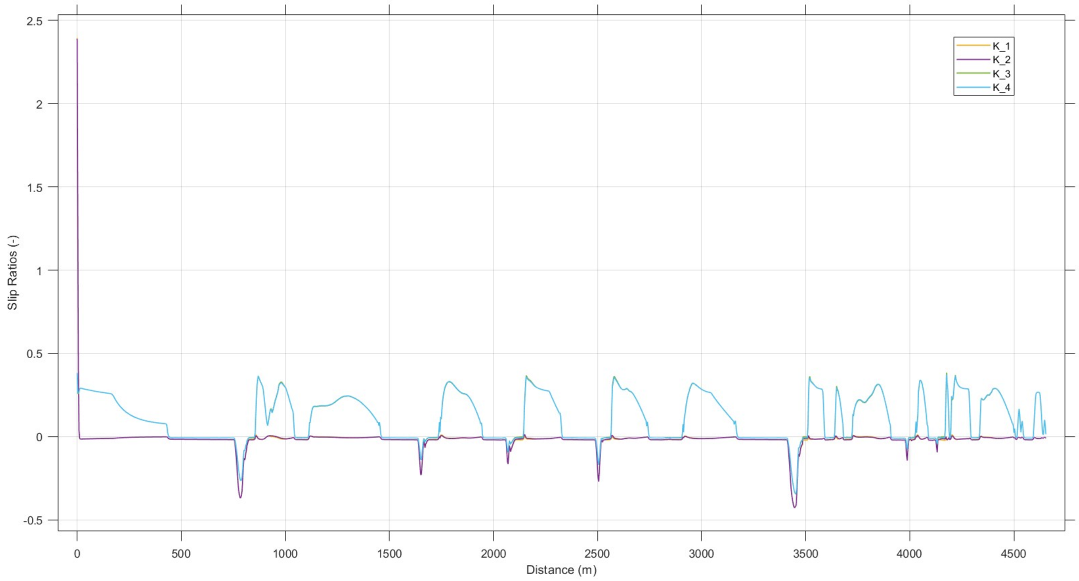

Figure 5.16: Slip ratios

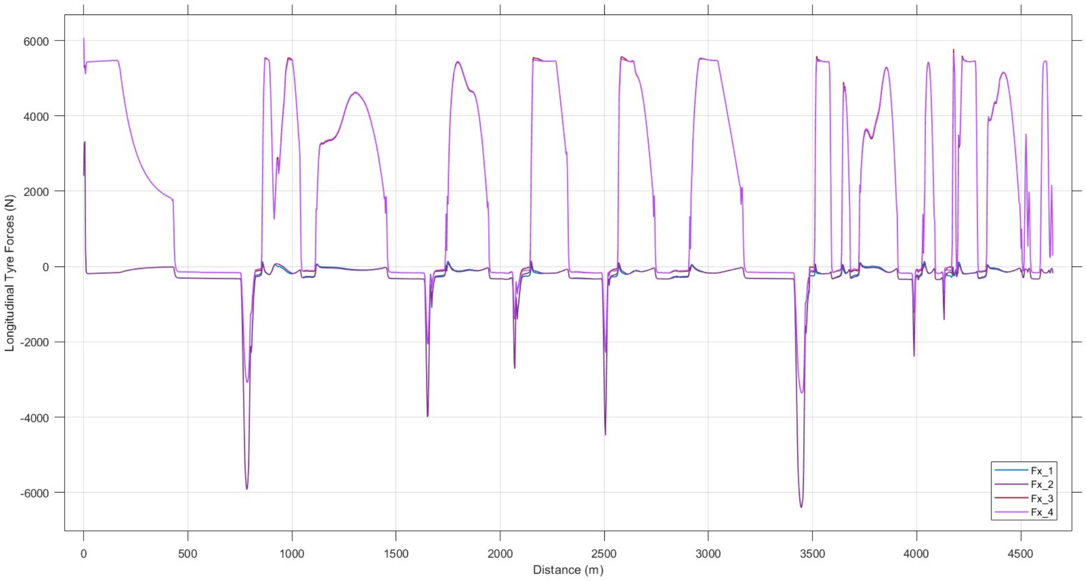

Figure 5.17: Longitudinal tyre forces

Interestingly, the improvement in driving torque is most prominent during turn 3 and turn 6. This suggests that Attack Mode has a more pronounced effect on driving torque during these cornering manoeuvres, potentially enabling drivers to carry more speed through these turns and enhance their overall lap times.

Figure 5.23 highlights the effect of engaging Attack Mode on the braking torque. When Attack Mode is activated, there is an increase in peak braking torque during corners following straights and fast corners, due to the higher achieved velocities. In these instances, where the driver attains maximum speed, there is an increased need to apply more braking force to slow the car down before entering the corner.

Conversely, during other corners, particularly the slower ones such as turn 14, the braking torque remains consistent regardless of Attack Mode activation. This demonstrates that Attack Mode

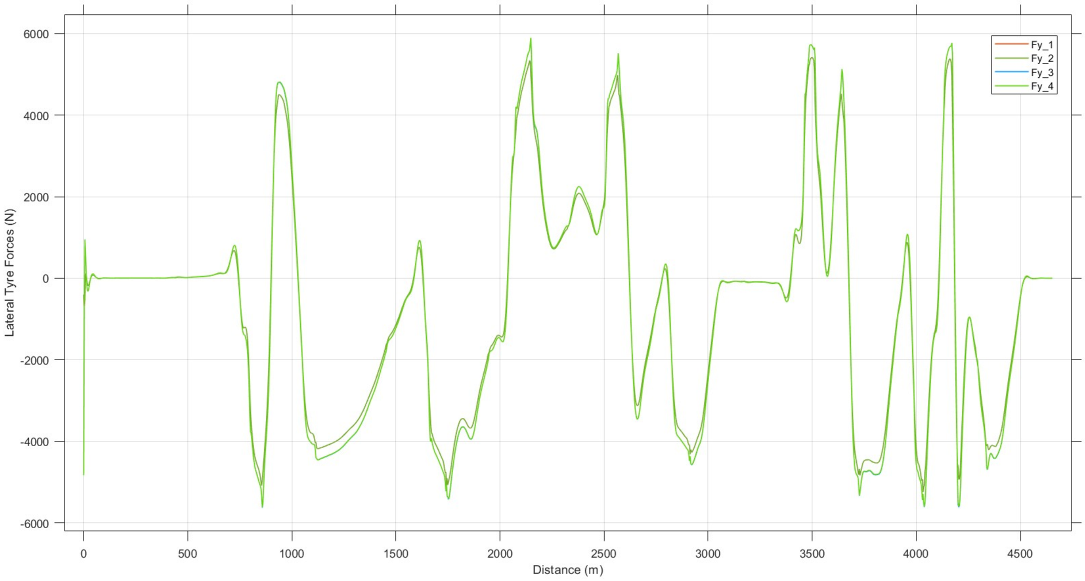

Figure 5.18: Lateral tyre forces

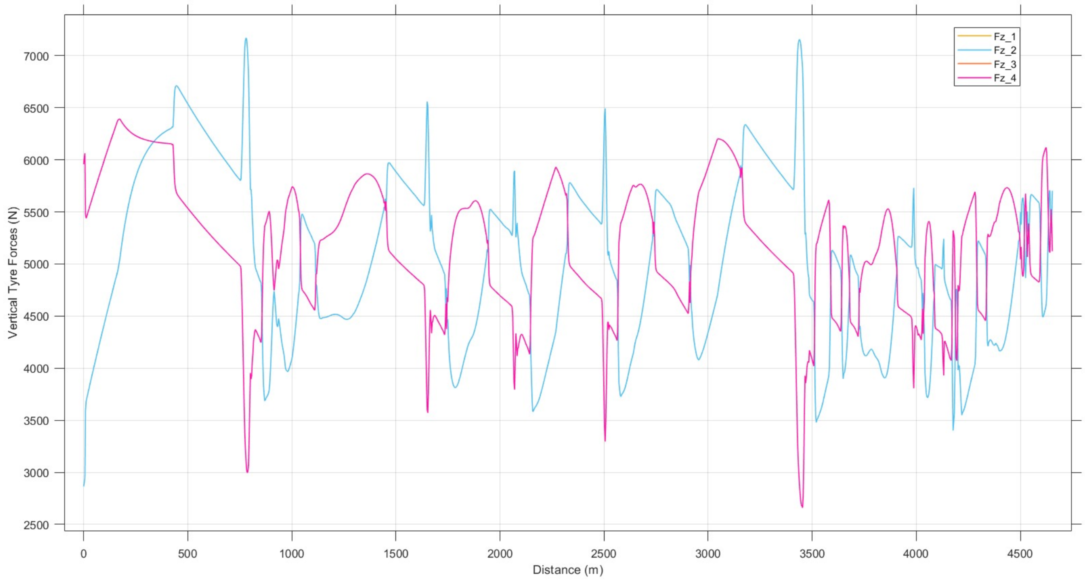

Figure 5.19: Vertical tyre forces

primarily influences braking torque in sections of the track where higher speeds are attained, while its impact is less pronounced in slower corners where braking requirements are less demanding.

Figure 5.24 illustrates the influence of activating Attack Mode on the regenerative braking torque. The graph shows that regenerative torque is similar for both cases. However, the main difference is in the last sector where the energy consumption is close to the limit thus more regenerative power is needed to not exceed the limit.

Figure 5.25 displays the changes in steering angle. The graph reveals that the car's trajectory closely follows the optimal racing line, with minimal deviations. This adherence to the racing line is expected, as it represents the most efficient path around the track.

However, subtle variations in steering angle are apparent, particularly noticeable at turn 1.

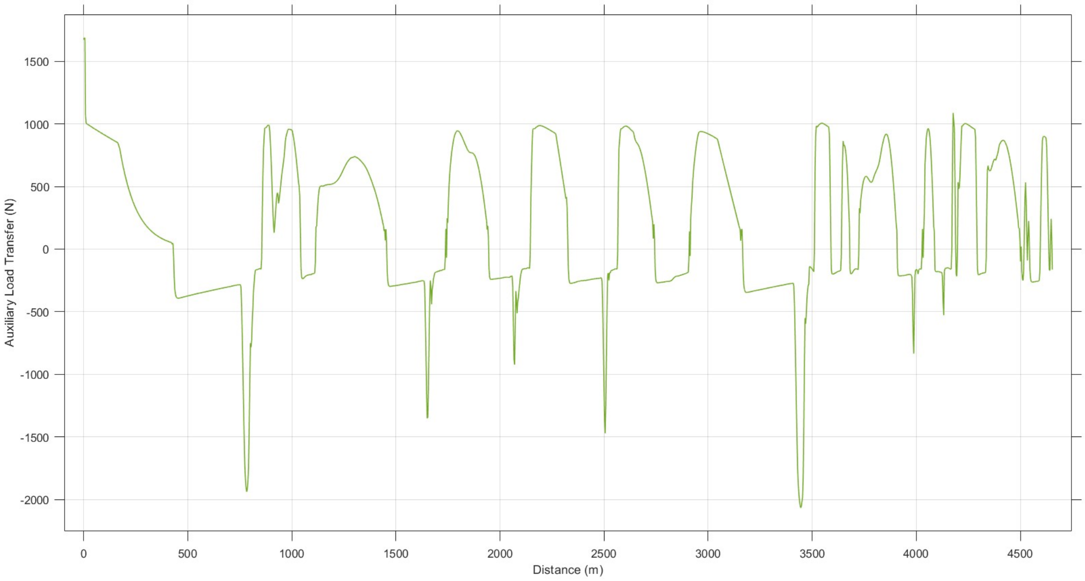

Figure 5.20: Auxiliary load transfer

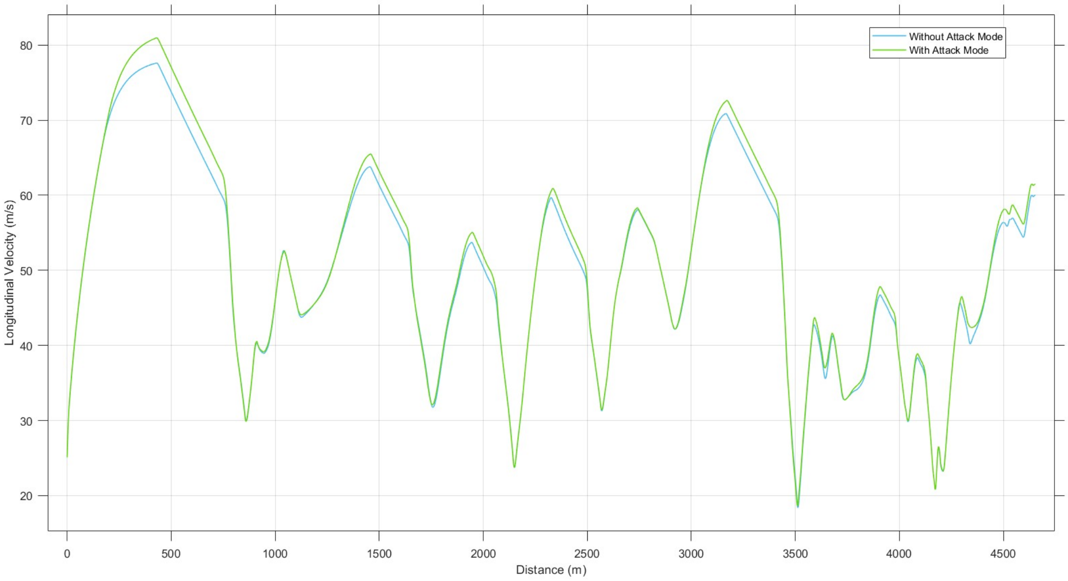

Figure 5.21: Comparison of longitudinal velocity

Here, the driver adjusts the steering angle slightly more to the right during Attack Mode. This adjustment is necessary due to the higher maximum speed attained when Attack Mode is activated, requiring the driver to make slight modifications to maintain control and follow the optimal racing line effectively. Overall, while the general shape of the car's trajectory remains consistent, these minor adjustments in steering angle highlight the dynamic nature of driving during Attack Mode.

Figure 5.26 demonstrates how the drag force increases significantly during Attack Mode activation. This increase is attributed to the higher speed of the car during Attack Mode, which leads to more drag.

This increased drag force is seen between the starting line and turn 1, as well as between turn 9 and turn 10, where long straight sections of the track allow the car to achieve higher velocities.

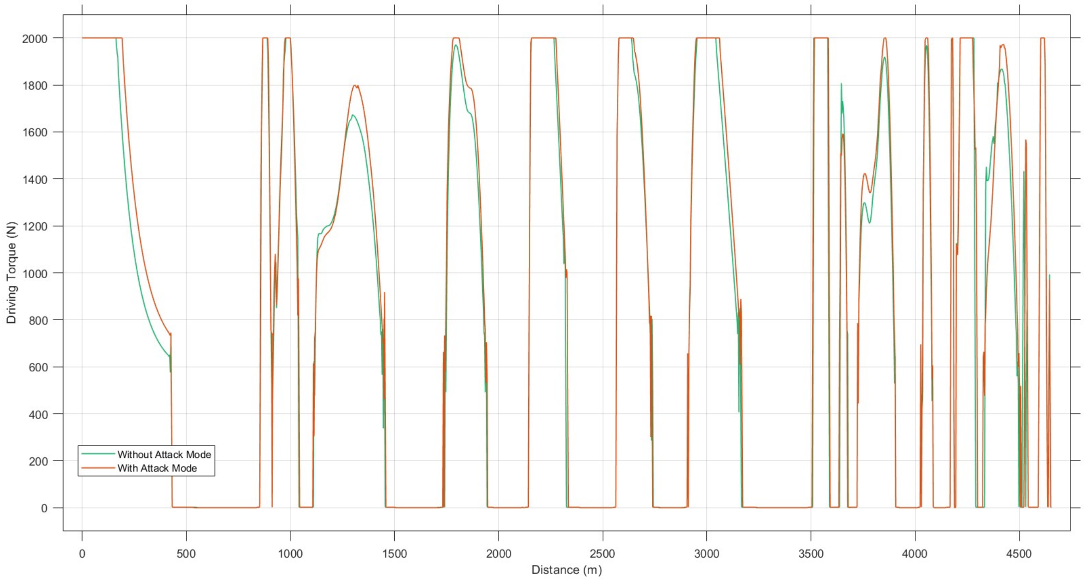

Figure 5.22: Comparison of driving torque

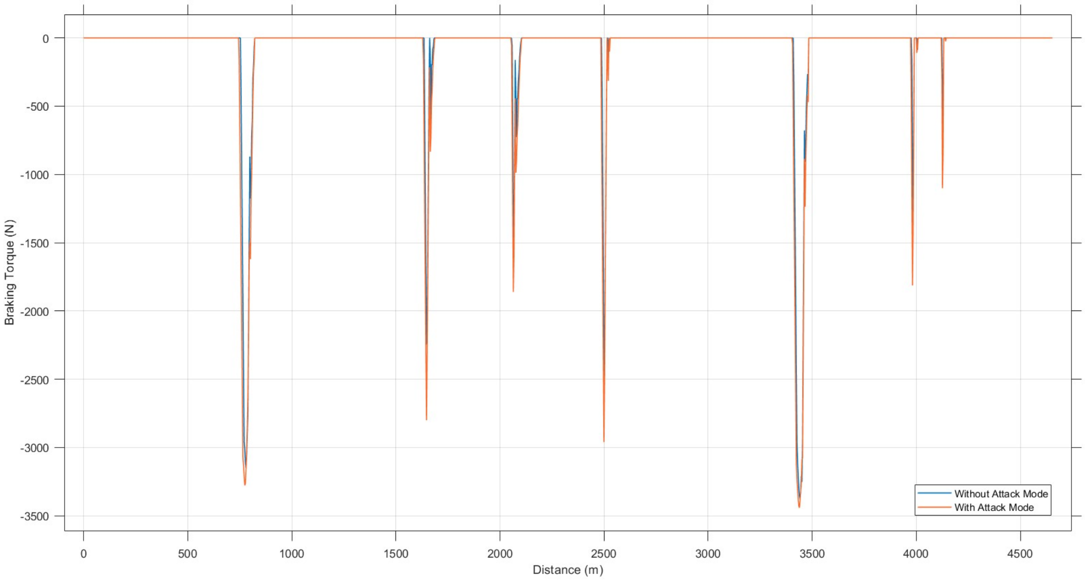

Figure 5.23: Comparison of braking torque

However, the drag force acting on the car remains relatively consistent throughout the rest of the lap, indicating that the significant increase observed during Attack Mode is primarily concentrated in the sections of the track characterized by high speeds.

Figure 5.27 depicts the variation in downforce between Attack Mode and non-Attack Mode conditions. The graph indicates that during Attack Mode, downforce is higher compared to when it is not activated. This increase in downforce is due to the car's higher speed during Attack Mode, as downforce typically increases with speed.

Both drag and downforce are dependent on the car's speed. As highlighted in Figure 5.26, during Attack Mode, when the car achieves higher speeds, there is a corresponding increase in downforce. This effect is seen between the starting line and turn 1, as well as between turn 9 and turn 10.

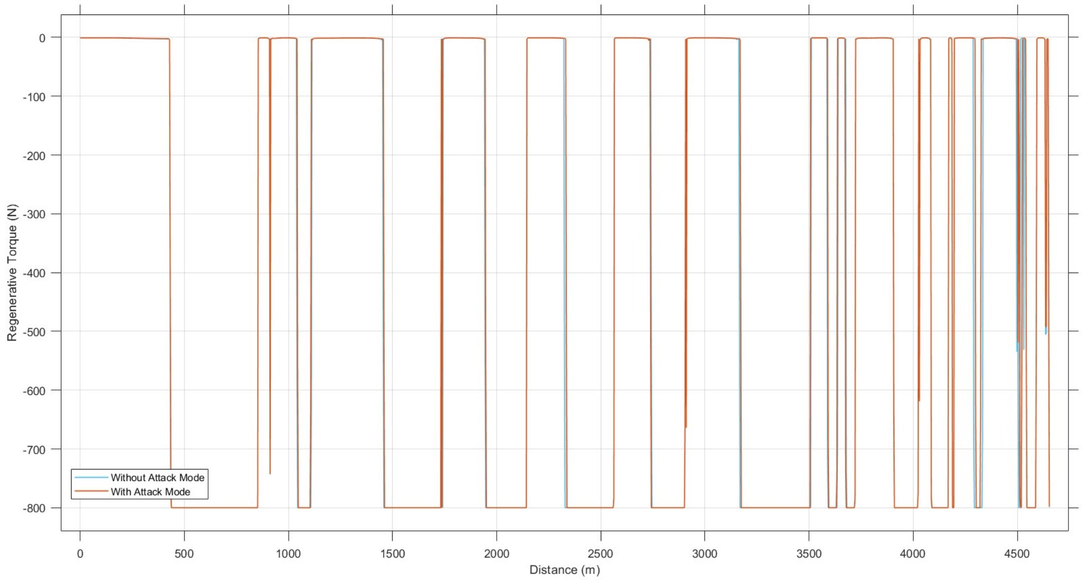

Figure 5.24: Comparison of regenerative torque

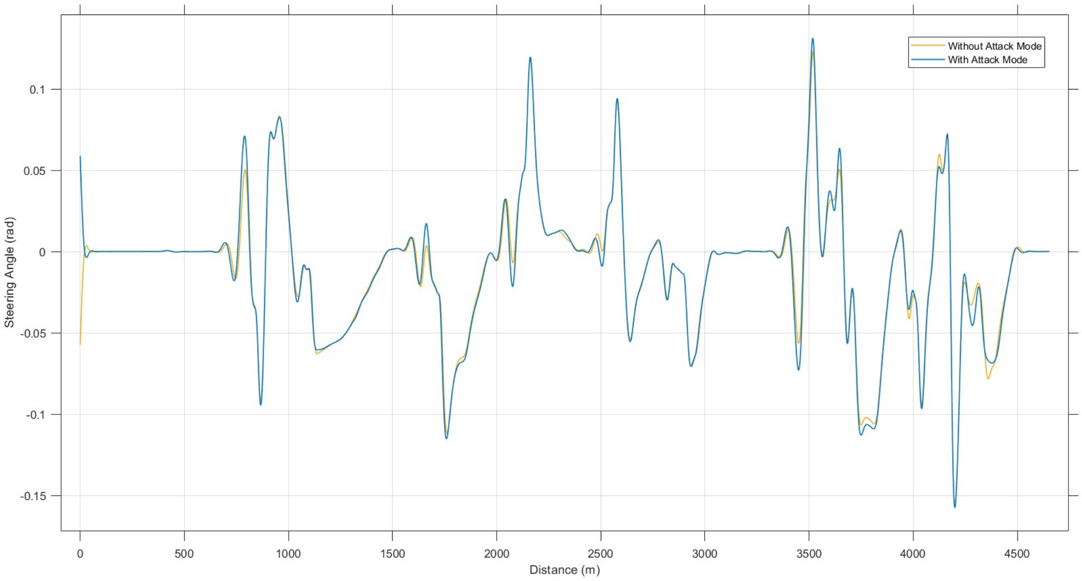

Figure 5.25: Comparison of steering angle

In contrast, in slower areas of the track, the downforce remains consistent, similar to non-Attack Mode conditions. This indicates that the significant increase in downforce observed during Attack Mode is primarily concentrated in faster sections of the track.

Figure 5.28 displays the car's energy consumption during the lap when Attack Mode is activated. Similarly, as illustrated in Figure 5.13, the largest consumption occurs over the longer first straight, before the first corner. The car then regenerates energy, allowing it to complete the lap while remaining under the maximum energy consumption restriction of 7.78e03 kJ (2.16 kWh). Furthermore, energy consumption is higher in the first and second sectors, with increased regeneration, especially during the quick corner at turn 3 and the straight stretch between turns 9 and 10. These areas require higher energy consumption due to the higher speeds resulting in increased energy regeneration.

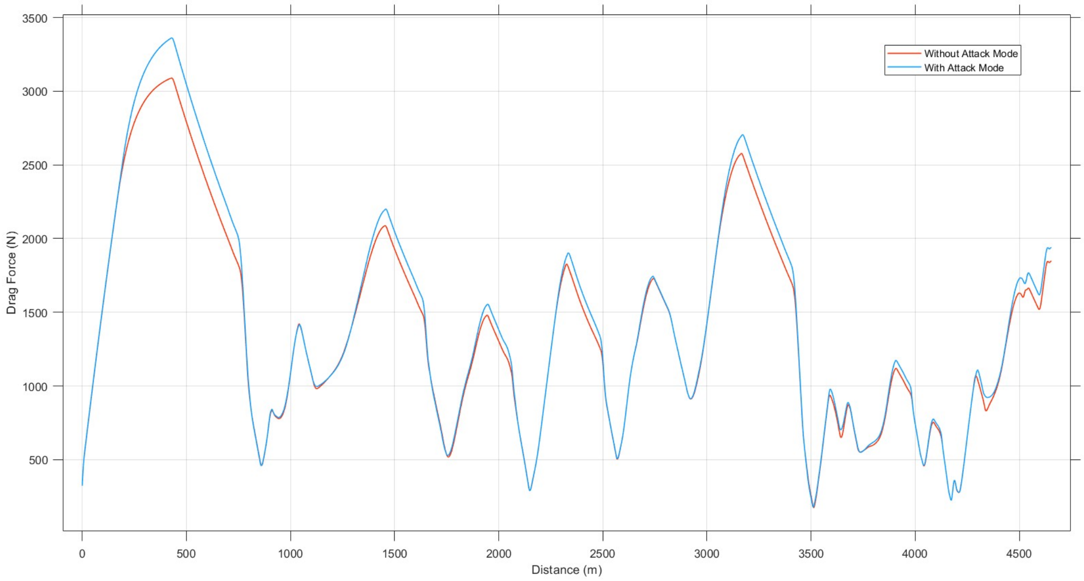

Figure 5.26: Comparison of drag force

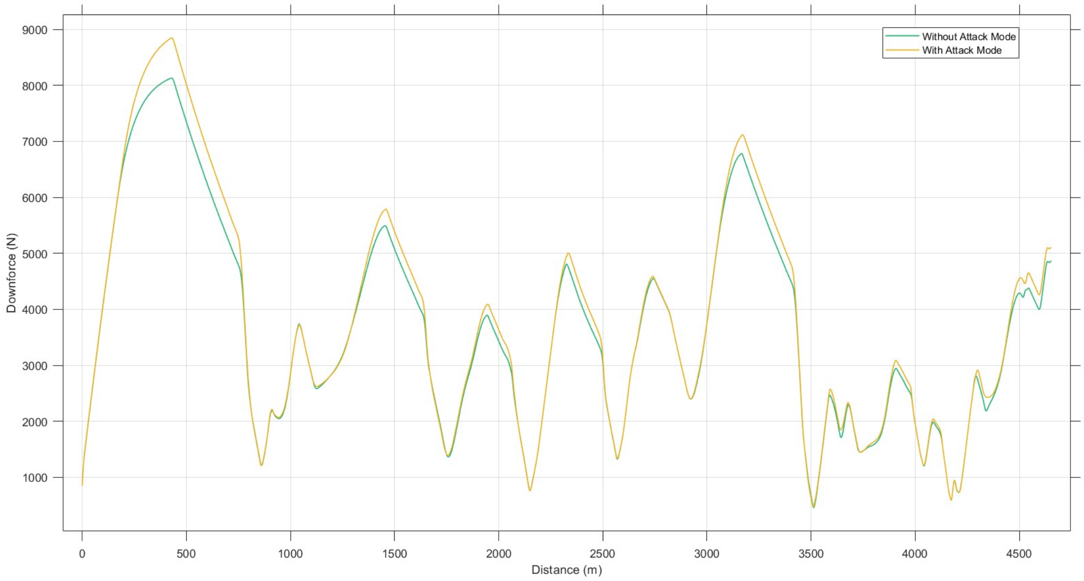

Figure 5.27: Comparison of downforce

Table 5.8 displays the difference during attack mode activation, indicating that increasing the power and energy restrictions reduces simulation running time.

Figures 5.29 and 5.30 show how the front and rear angular velocities vary during the Attack Mode. Figure 5.31 indicates the changes in slip angles, whereas Figure 5.32 depicts the slip ratios of the tyres. Figure 5.33 illustrates the lateral velocity. Figures 5.34, 5.35, and 5.36 show the longitudinal, lateral, and vertical tyre forces, respectively. Finally, Figure 5.37 illustrates auxiliary load transfers.

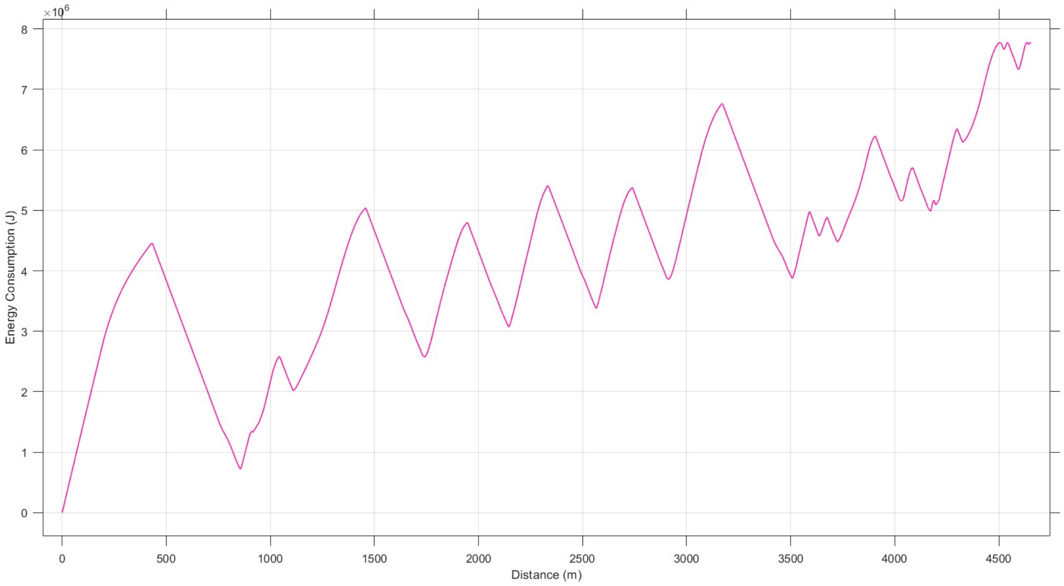

Figure 5.28: Energy consumption during Attack Mode

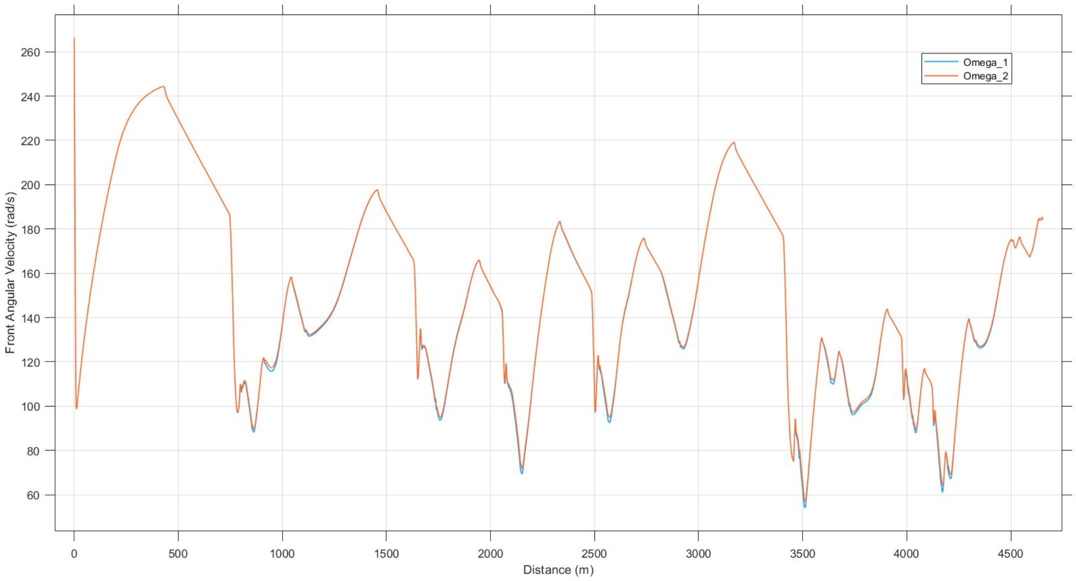

Figure 5.29: Front angular velocities during Attack Mode

5.5 Energy Consumption

This section examines how energy restrictions impact the car's performance. Figure 5.38 illustrates the correlation between energy restrictions and track speed, based on the original energy per lap allocation of 1.6 kWh during racing mode. A noticeable effect emerges: with reduced available energy, the optimal solution for minimizing lap time tends to prioritize cuts in high-speed sections. Consequently, the car begins to decelerate before reaching its potential maximum speed, particularly evident when the energy restriction is lowered. Remarkably, a substantial improvement is observed at 194.4e+3 kJ (54 kWh) of available energy, whereas minor differences are noted with slight energy increases, primarily evident in straight-line stretches and fast corners. On the other hand, reducing energy below the simulation's baseline leads to more pronounced differences, noticeably apparent on long straights and during both fast and slow corners.

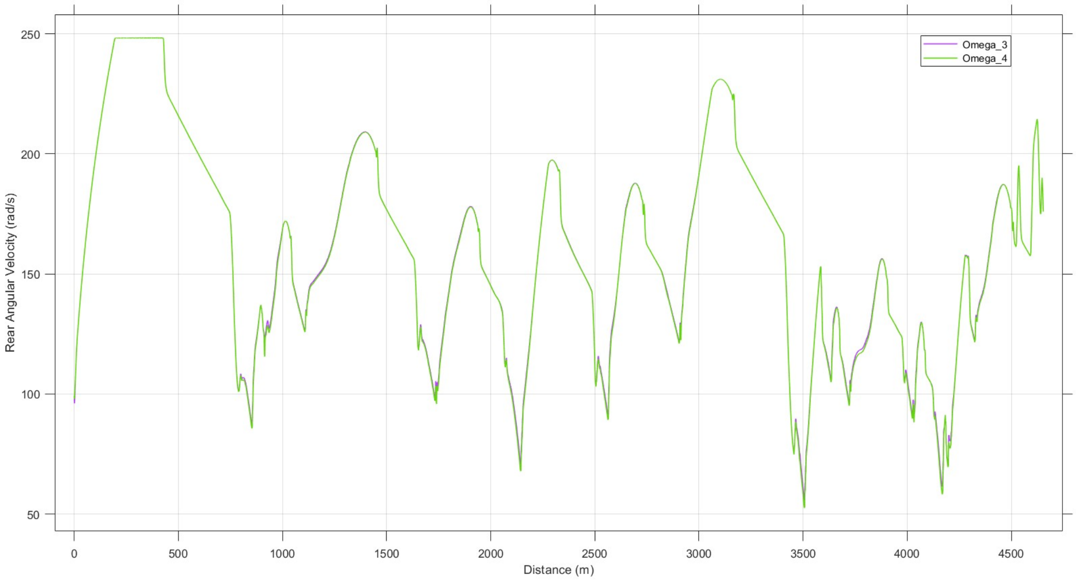

Figure 5.30: Rear angular velocities during Attack Mode

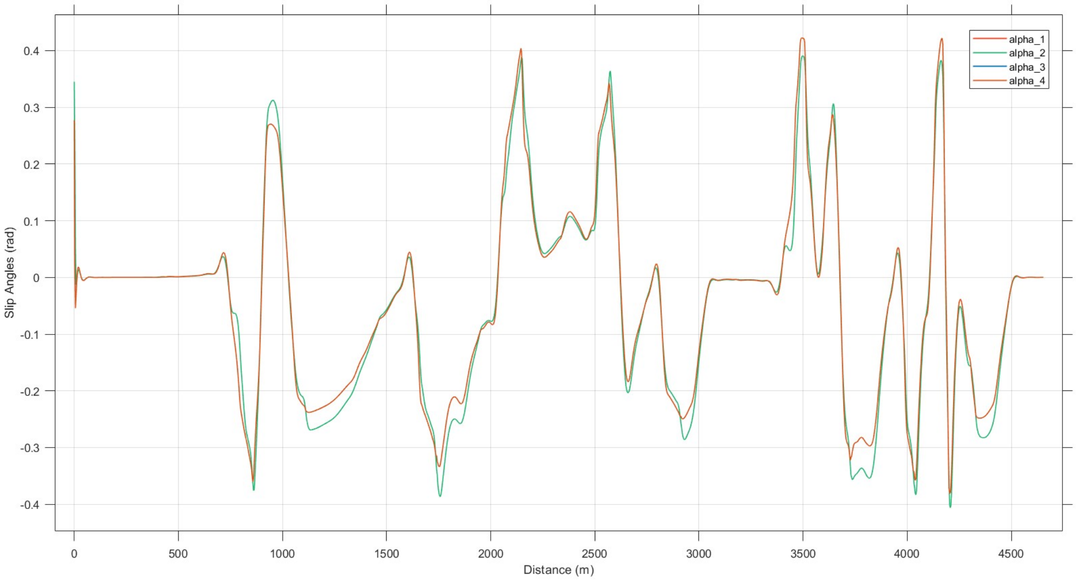

Figure 5.31: Slip angles during Attack Mode

Figure 5.39 illustrates the difference between the variation of the energy consumption with and without attack mode activation. It is possible to see that the energy consumption has the same trend for both but with higher energy consumption for the attack mode due to the increase of the energy consumption limit from 5.76e+3 kJ (1.6 kWh) to 7.78e+3 kJ (2.16 kWh).

Table 5.9 shows the difference during different energy consumption limits, showing that increasing the energy restrictions reduces the lap time as well as the simulation running time.

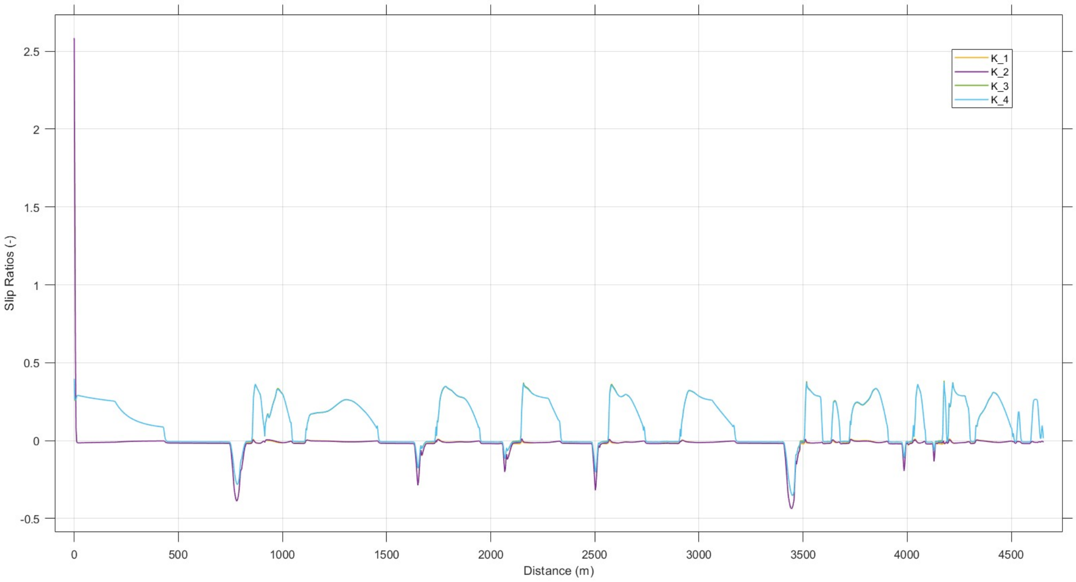

Figure 5.32: Slip ratio during Attack Mode

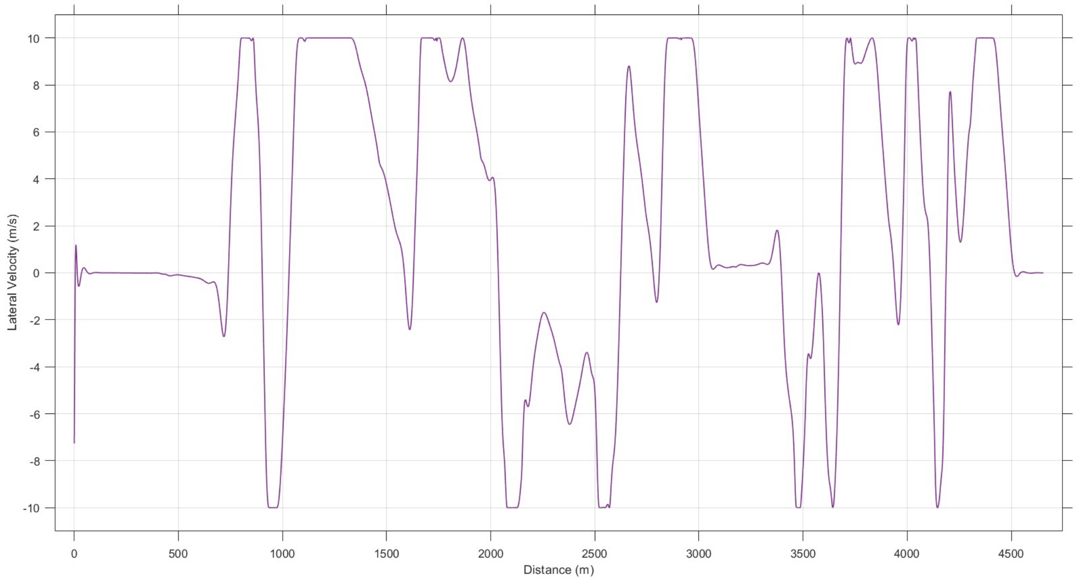

Figure 5.33: Lateral velocity during Attack Mode

Table 5.8: Simulation results with and without Attack Mode activation

Attack Mode	Maximum Speed [m/s]	Lap Time [s]	Simulation Time [s]
OFF	77.6	96.338	2952.7
ON	80.9	95.033	1618.1

Table 5.9: Simulation results with and different energy limits

Energy Constraints[kWh]	Maximum Speed[m/s]	Lap Time[s]	Simulation Time[s]
0.9	73	98.412	3096.5
1.6	77.6	96.338	2952.7
2.3	77.9	95.028	2098.8
54	78.3	90.219	964.5

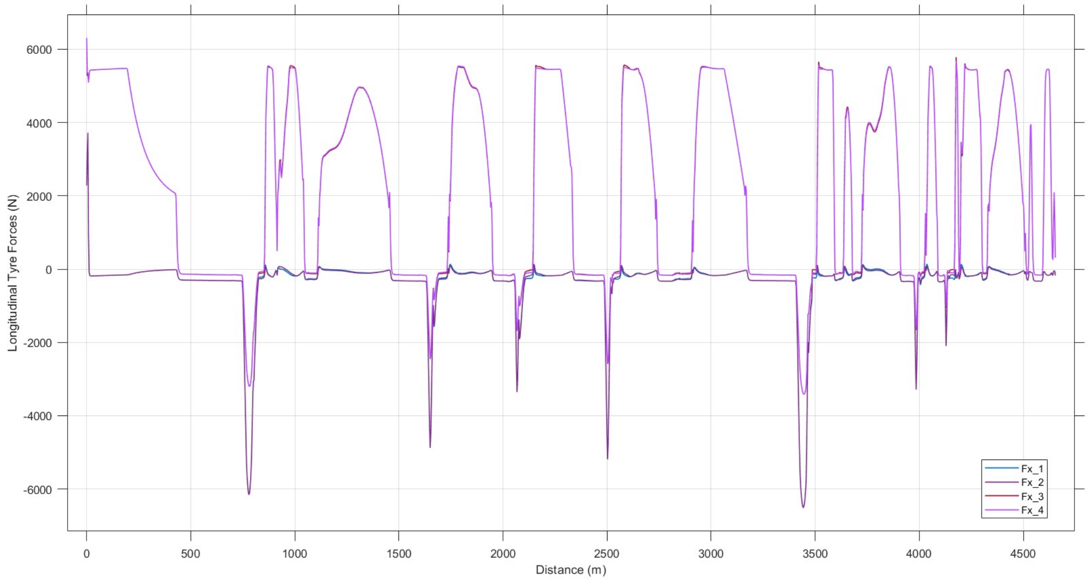

Figure 5.34: Longitudinal tyre forces during Attack Mode

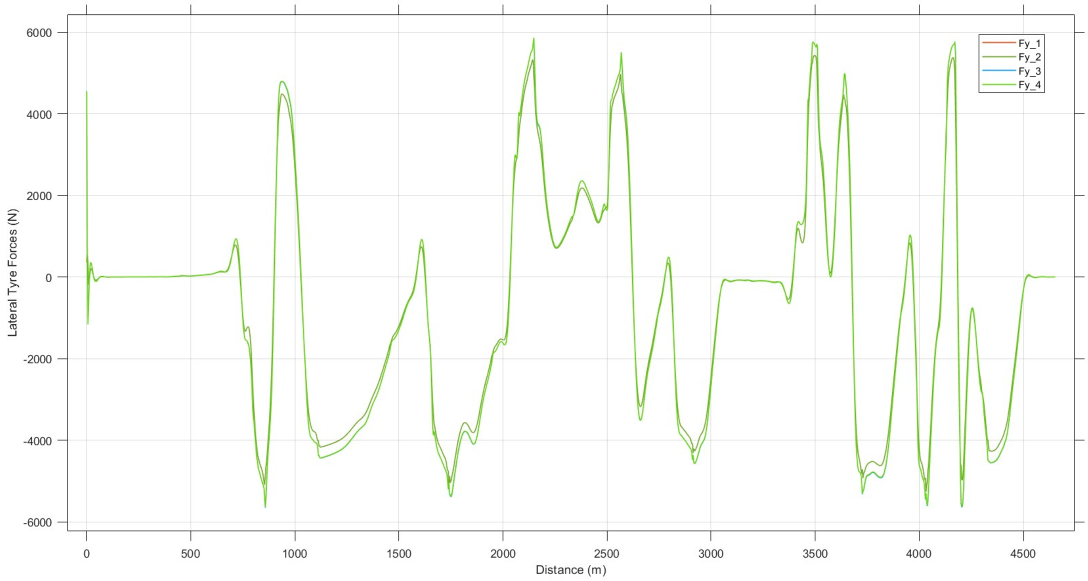

Figure 5.35: Lateral tyre forces during Attack Mode

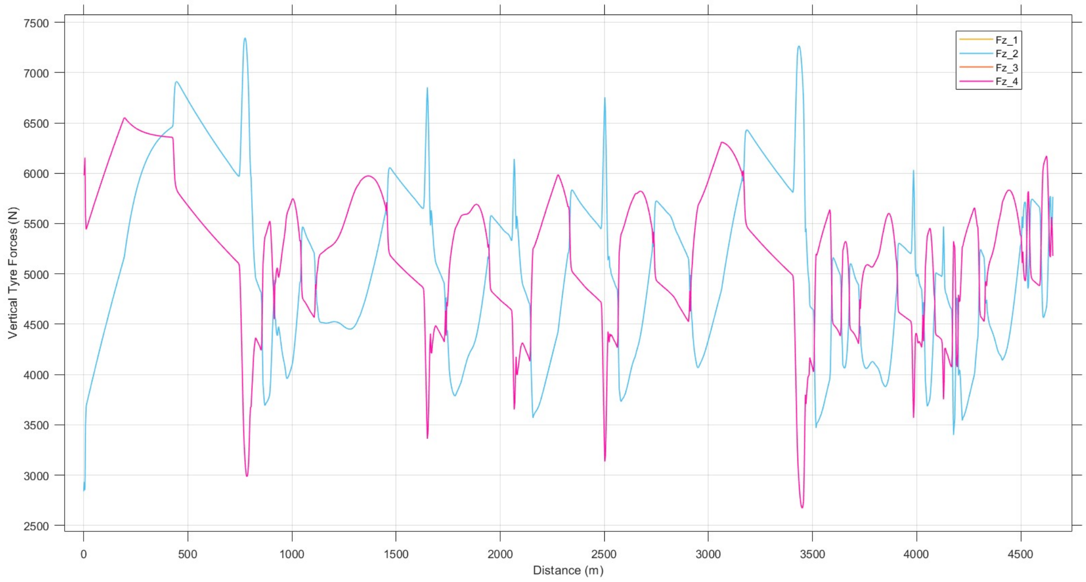

Figure 5.36: Vertical tyre forces during Attack Mode

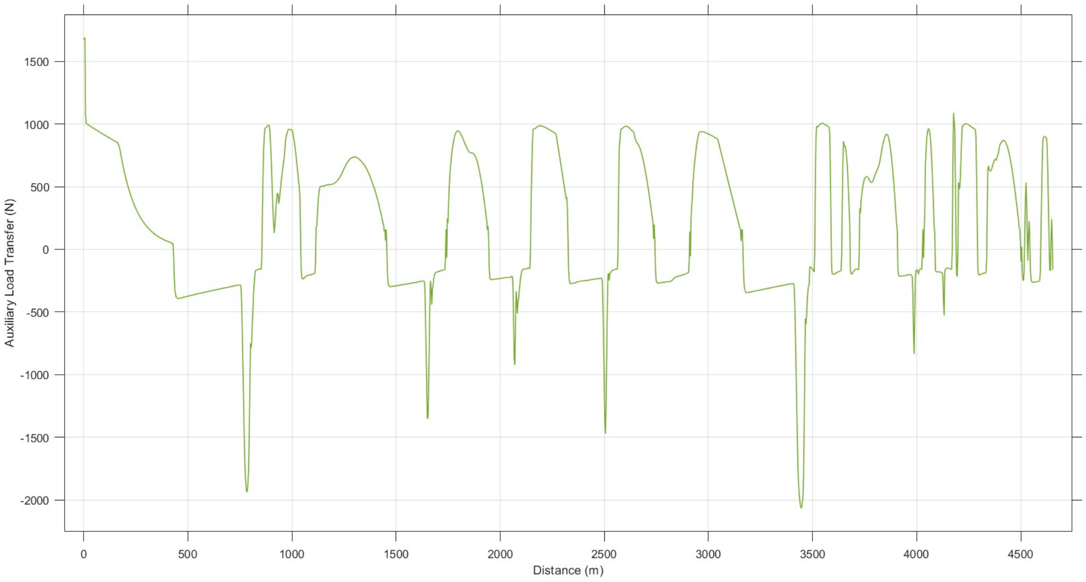

Figure 5.37: Auxiliary load transfer during Attack Mode

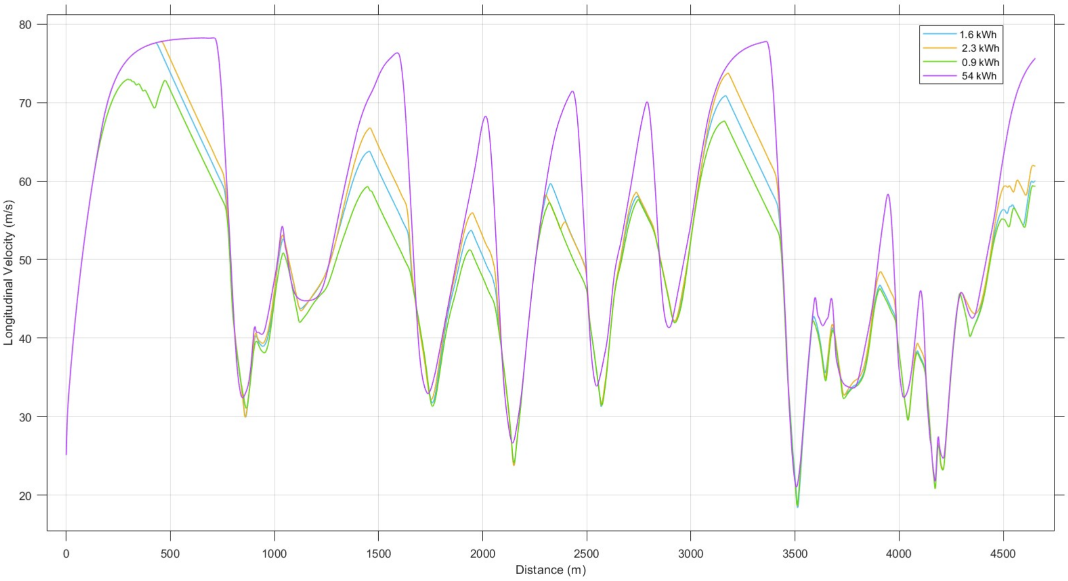

Figure 5.38: Velocity profiles with different energy consumption limitations

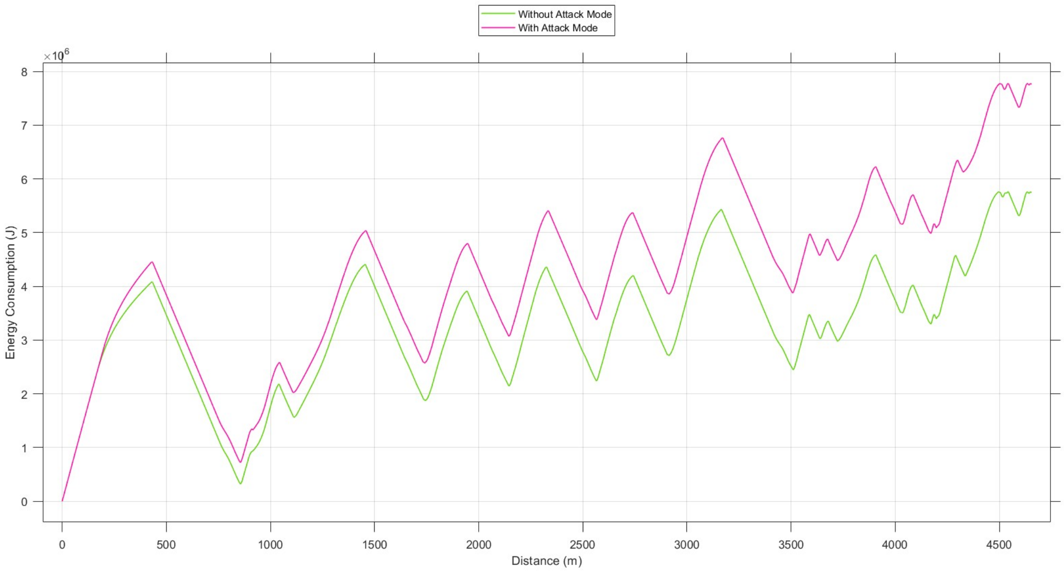

Figure 5.39: Energy consumption difference during the activation of Attack Mode

Chapter 6

Conclusion

In this thesis, a racing strategy simulation was conducted for a Formula E car operating under energy constraints. Using Matlab, the simulation parameters and variables were provided to Casadi to solve the nonlinear problem (NLP) and determine the minimum lap time under varying energy consumption scenarios on the Circuit de Barcelona. The parameters utilized in this study were obtained from publicly available data rather than directly from the Formula E team, yielding satisfactory results.

The simulation environment was characterized by a track model represented in a curvilinear coordinate system and a vehicle model with seven degrees of freedom (DOFs), incorporating aerodynamic loads, load transfer, limited-slip differential (LSD), and an empirical tire model for wheel dynamics.

The controller aspect of this work involved enhancing a previously developed controller with additional functionalities beyond trajectory following. This included optimizing the racing line trajectory to minimize lap time through trajectory optimization. Direct orthogonal local collocation with barycentric Lagrange interpolation was employed to store and assess high-order orthogonal polynomials. State and control variable scaling was utilized to enhance optimization algorithm efficiency, while input derivatives, including second derivatives, were added as penalty terms to mitigate oscillation and convergence issues. Initial guesses were also adjusted to expedite simulation time by simplifying the model and employing linear tyres with increased collocation steps.

The final part of this work presented the optimization results for the racing line and the simulation setup used. The analysis delved into the results of the race mode regarding state and control variables, the impact of activating the Attack Mode, and the energy consumption differences between various energy restrictions and race modes. The optimal lap time was obtained respecting the energy consumption limits with and without the activation of the Attack Mode.

Overall, this thesis highlights the importance of modelling activities in capturing essential vehicle dynamics aspects to improve performance. The selection of model equations and optimization problem variables significantly influences solver convergence and computational efficiency. Balancing model complexity is crucial to achieving an optimal compromise between computational efficiency and accuracy, ultimately enabling realistic behaviour capture and Formula E car optimization.

Bibliography

[1] Nicolas Mauduit and G Pastor. «Venturi Formula E Team in the 100% Electric New FIA Championship». In: *15. Internationales Stuttgarter Symposium: Automobil-und Motorentechnik*. Springer. 2015, pp. 1127–1127 (cit. on p. 1).

[2] Giorgio Rizzoni, D Cooke, and G Pastor. «The fastest electric vehicles on earth: A history of electric land speed racing and of the Venturi Buckeye Bullet program». In: *15. Internationales Stuttgarter Symposium: Automobil-und Motorentechnik*. Springer. 2015, pp. 1129–1130 (cit. on p. 1).

[3] Willem Standaert and Sirkka Jarvenpaa. «Formula E: Next generation motorsport with next generation fans». In: *International Conference on Information Systems*. 2016 (cit. on pp. 1, 2).

[4] *2023-24 S10 FIA Formula E World Championship Technical Regulations*. URL: `https://www.fia.com/regulation/category/109` (cit. on p. 1).

[5] FIA Formula E. *Gen1 To Gen3: The Evolution Of EVs In Formula E*. 2022. URL: `www.fiaformulae.com/en/news/1733/gen1-to-gen3-the-evolution-of-evs-in-formula-e` (cit. on pp. 1, 33).

[6] Xuze Liu, Abbas Fotouhi, and Daniel J Auger. «Optimal energy management for formula-E cars with regulatory limits and thermal constraints». In: *Applied Energy* 279 (2020), p. 115805 (cit. on pp. 1, 7, 9, 10).

[7] Unnatee Gidithuri. *Formula E: All you need to know*. 2023. URL: `www.autocarindia.com/motor-sports-news/balu-wins-11th-national-title-sanjay-crowned-mrf-f2000-champion-427137` (cit. on pp. 2–5).

[8] Joel AE Andersson, Joris Gillis, Greg Horn, James B Rawlings, and Moritz Diehl. «CasADi: a software framework for nonlinear optimization and optimal control». In: *Mathematical Programming Computation* 11 (2019), pp. 1–36 (cit. on p. 2).

[9] Andreas Wächter and Lorenz T Biegler. «On the implementation of an interior-point filter line-search algorithm for large-scale nonlinear programming». In: *Mathematical programming* 106 (2006), pp. 25–57 (cit. on p. 2).

[10] Rich Opong. *What Is Formula E Attack Mode? (All You Need To Know)*. 2021. URL: `https://flowracers.com/blog/formula-e-attack-mode/` (cit. on pp. 4, 5).

[11] FIA Formula E. *RULES AND REGULATIONS*. URL: `https://www.fiaformulae.com/en/championship/rules-and-regulations` (cit. on p. 4).

[12] H Scherenberg. «Mercedes-benz racing cars—design and experience». In: *SAE Transactions* (1958), pp. 414–420 (cit. on p. 6).

[13] Blake Siegler, Andrew Deakin, and David Crolla. «Lap time simulation: Comparison of steady state, quasi-static and transient racing car cornering strategies». In: *SAE transactions* (2000), pp. 2575–2581 (cit. on p. 6).

[14] DL Brayshaw and MF Harrison. «A quasi steady state approach to race car lap simulation in order to understand the effects of racing line and centre of gravity location». In: *Proceedings of the Institution of Mechanical Engineers, Part D: Journal of Automobile Engineering* 219.6 (2005), pp. 725–739 (cit. on p. 6).

[15] Daniele Casanova. «On minimum time vehicle manoeuvring: The theoretical optimal lap». In: (2000) (cit. on p. 6).

[16] Daniel Patrick Kelly. «Lap time simulation with transient vehicle and tyre dynamics». PhD thesis. Cranfield University Cranfield, 2008 (cit. on pp. 6, 12).

[17] Timo Völkl. *Erweiterte quasistatische Simulation zur Bestimmung des Einflusses transienten Fahrzeugverhaltens auf die Rundenzeit von Rennfahrzeugen.* Vol. 83. Cuvillier Verlag, 2013 (cit. on p. 6).

[18] Julian Timings and David Cole. «Robust lap-time simulation». In: *Proceedings of the institution of mechanical engineers, part D: journal of automobile engineering* 228.10 (2014), pp. 1200–1216 (cit. on p. 6).

[19] Giacomo Perantoni and David JN Limebeer. «Optimal control of a formula one car on a three-dimensional track—Part 1: Track modeling and identification». In: *Journal of Dynamic Systems, Measurement, and Control* 137.5 (2015), p. 051018 (cit. on pp. 6, 7).

[20] David JN Limebeer and Giacomo Perantoni. «Optimal control of a formula one car on a three-dimensional track—Part 2: Optimal control». In: *Journal of Dynamic Systems, Measurement, and Control* 137.5 (2015), p. 051019 (cit. on p. 6).

[21] Enrico Bertolazzi, Francesco Biral, and Mauro Da Lio. «Symbolic-numeric efficient solution of optimal control problems for multibody systems». In: *Journal of computational and applied mathematics* 185.2 (2006), pp. 404–421 (cit. on p. 6).

[22] Bobbo Simon, Cossalter Vittore, Massaro Matteo, and Peretto Martino. «Application of the "optimal maneuver method" for enhancing racing motorcycle performance». In: *SAE International Journal of Passenger Cars-Mechanical Systems* 1.2008-01-2965 (2008), pp. 1311–1318 (cit. on p. 6).

[23] Vittore Cossalter, Roberto Lot, and Davide Tavernini. «Optimization of the centre of mass position of a racing motorcycle in dry and wet track by means of the "optimal maneuver method"». In: *2013 IEEE International Conference on Mechatronics (ICM).* IEEE. 2013, pp. 412–417 (cit. on p. 6).

[24] Davide Tavernini, Matteo Massaro, Efstathios Velenis, Diomidis I Katzourakis, and Roberto Lot. «Minimum time cornering: the effect of road surface and car transmission layout». In: *Vehicle System Dynamics* 51.10 (2013), pp. 1533–1547 (cit. on p. 6).

[25] Davide Tavernini, Efstathios Velenis, Roberto Lot, and Matteo Massaro. «The optimality of the handbrake cornering technique». In: *Journal of Dynamic Systems, Measurement, and Control* 136.4 (2014), p. 041019 (cit. on p. 6).

[26] Christian Kirches, Sebastian Sager, Hans Georg Bock, and Johannes P Schlöder. «Time-optimal control of automobile test drives with gear shifts». In: *Optimal Control Applications and Methods* 31.2 (2010), pp. 137–153 (cit. on p. 6).

[27] Michael A Patterson and Anil V Rao. «GPOPS-II: A MATLAB software for solving multiple-phase optimal control problems using hp-adaptive Gaussian quadrature collocation methods and sparse nonlinear programming». In: *ACM Transactions on Mathematical Software (TOMS)* 41.1 (2014), pp. 1–37 (cit. on p. 6).

[28] David JN Limebeer, Giacomo Perantoni, and Anil V Rao. «Optimal control of formula one car energy recovery systems». In: *International Journal of Control* 87.10 (2014), pp. 2065–2080 (cit. on p. 6).

[29] Mehdi Imani Masouleh and David JN Limebeer. «Optimizing the aero-suspension interactions in a formula one car». In: *IEEE Transactions on Control Systems Technology* 24.3 (2015), pp. 912–927 (cit. on pp. 6, 9).

[30] Vittore Cossalter, Mauro Da Lio, Roberto Lot, and Lucca Fabbri. «A general method for the evaluation of vehicle manoeuvrability with special emphasis on motorcycles». In: *Vehicle system dynamics* 31.2 (1999), pp. 113–135 (cit. on p. 7).

[31] Fabian Christ, Alexander Wischnewski, Alexander Heilmeier, and Boris Lohmann. «Time-optimal trajectory planning for a race car considering variable tyre-road friction coefficients». In: *Vehicle system dynamics* 59.4 (2021), pp. 588–612 (cit. on p. 9).

[32] Roberto Lot and Francesco Biral. «A curvilinear abscissa approach for the lap time optimization of racing vehicles». In: *IFAC Proceedings Volumes* 47.3 (2014), pp. 7559–7565 (cit. on p. 9).

[33] Hans Pacejka. *Tire and vehicle dynamics*. Elsevier, 2005 (cit. on p. 12).

[34] Nicola Dal Bianco, Enrico Bertolazzi, Francesco Biral, and Matteo Massaro. «Comparison of direct and indirect methods for minimum lap time optimal control problems». In: *Vehicle System Dynamics* 57.5 (2019), pp. 665–696 (cit. on p. 17).

[35] Anil V Rao. «A survey of numerical methods for optimal control». In: *Advances in the astronautical Sciences* 135.1 (2009), pp. 497–528 (cit. on p. 17).

[36] Jean-Paul Berrut and Lloyd N Trefethen. «Barycentric lagrange interpolation». In: *SIAM review* 46.3 (2004), pp. 501–517 (cit. on pp. 19, 20).

[37] *Formula 1 Gran Premio De Espana 2021*. URL: `https://www.team-bhp.com/forum/intl-motorsport/236647-formula-1-2021-spanish-grand-prix-7-9-may.html` (cit. on p. 27).

[38] *Circuit de Barcelona-Catalunya*. URL: `https://commons.wikimedia.org/wiki/File:Formula1_Circuit_Catalunya.svg` (cit. on p. 27).